Politecnico di Torino

Mechatronic Engineering

A.a. 2025/2026

Graduation Session July 2026

Finite Element Evaluation of Eddy-Current Losses in the Permanent Magnets of Coaxial Magnetic Gears

Supervisor:
Prof. MAURIZIO REPETTO

Candidate:
GIUSEPPE PETROLITO

Acknowledgements

First and foremost, I would like to express my sincere gratitude to Professor Maurizio Repetto for the opportunity he gave me, as well as for his availability, guidance, and continuous support throughout the development of this thesis.

I would also like to thank my parents, who have supported me with patience and trust throughout my entire academic journey. Their constant encouragement has been fundamental in helping me achieve this accomplishment.

Table of Contents

List of Tables

List of Figures

Acronyms

BM buried magnet

CMG coaxial magnetic gear

EMT electromagnetic torque

FEM finite element method

MG-PMSM magnetic geared permanent magnet synchronous motor

PM permanent magnet

SM surface magnet

Chapter 1

Introduction to coaxial magnetic gears (CMGs)

This chapter introduces the fundamental advantages of magnetic gears with respect to their conventional mechanical counterparts. Particular attention is devoted to coaxial magnetic gears (CMGs), whose operating principle and main characteristics are presented.

The chapter subsequently provides an overview of the different CMG topologies reported in the literature, highlighting how variations in structural features, such as magnet arrangement, magnetization distribution, and flux-coupling direction, influence the overall design and performance of the device.

Finally, several industrial applications of CMGs are reviewed, illustrating their adoption in magnetic gearboxes, renewable energy conversion systems, and integrated electromechanical drive solutions. These examples demonstrate the potential of CMGs as a reliable and efficient alternative to traditional mechanical transmission technologies.

1.1 Overview magnetic gears

The increasing demand for high-efficiency power transmission systems, together with the technological progress achieved in the development of materials characterized by high residual magnetization, has promoted the emergence of magnetic gears as a valid alternative to conventional mechanical gear topologies.

Figure 1.1 illustrates several magnetic counterparts of traditional mechanical transmission systems.

Magnetic gear solutions based on permanent magnets (PMs) enable contactless torque transmission, thereby overcoming several limitations typically associated with conventional mechanical gears. In particular, the absence of physical contact between moving parts eliminates friction phenomena, which in mechanical systems lead to progressive wear of the gear teeth and consequently reduce the capability of transmitting forces and torque over time.

Furthermore, magnetic gears do not require lubrication systems, which are conventionally adopted both to reduce friction and to provide thermal cooling of the gears. Additional advantages include a significant reduction in mechanical vibrations and acoustic noise during operation.

Magnetic gears also introduce intrinsic overload protection capabilities. When the transmitted torque exceeds the maximum transmissible value, the magnetic coupling is lost and the rotors simply slip relative to each other, avoiding mechanical damage. Consequently, external torque-limiting devices are generally not required.

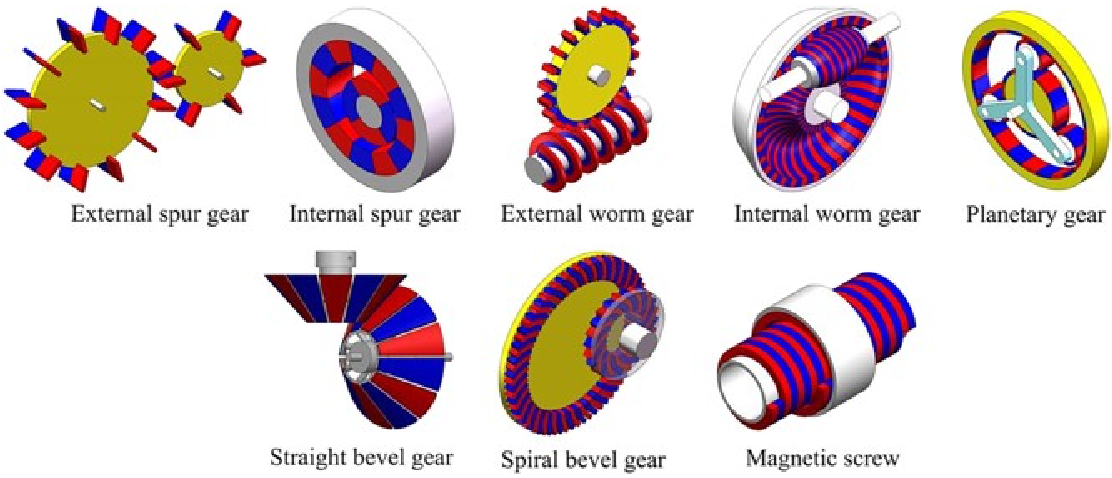

Figure 1.1: Magnetic alternatives of conventional mechanical gear topologies [1].

Although regarding torque transmission, magnetic gears generally exhibit a lower torque density than their conventional mechanical counterparts, in regards of planetary gears, a design of CMG offers comparable performance of its mechanical counter parts that have been progressively integrated into transmission gearboxes and PM electrical machines. Moreover, several hybrid configurations combining magnetic gears and electrical machines have been proposed in literature to realize high torque-density pseudo direct-drive systems [2].

By integrating the magnetic gear and the electrical machine within a single electromagnetic structure, these solutions can simultaneously provide speed reduction, torque amplification, and electromechanical energy conversion, while maintaining the inherent advantages of magnetic gear, such as reduced maintenance, improved reliability, and overload protection [2].

1.2 Types of CMGs

CMGs are composed of two concentric rotors carrying arrays of PMs and a magnetic field modulator positioned between them [3], [4].

More specifically, assuming the outer rotor as the output member, the magnetic field generated by the inner rotor is modulated by the ferromagnetic pole pieces of the intermediate rotor. This modulation process enables the interaction between the magnetic fields produced by the inner and outer rotors, thus allowing torque transmission.

Examples of CMGs are reported in Figure 1.2.

Henceforth, the three main components of the magnetic gear will be identified as follows:

- Inner rotor: Sun;
- Middle rotor: Carrier;
- Outer rotor: Ring.

The various coaxial magnetic gear topologies proposed in the literature can be classified according to the following structural features:

1. Mounting arrangement of the PMs within the rotors;
2. Magnetic field distribution generated by the rotors (tangential or radial);
3. Magnetic coupling direction (radial-flux or axial-flux).

Figures 1.2a, 1.2b, 1.2c illustrates examples of the first two classification criteria. These variations may also be adopted only on one rotor, providing significant flexibility in the selection of the most suitable topology according to the required operational performance. The PMs are represented using different colors (red and blue), while the arrows inside them indicate the magnetization direction.

Considering first the mounting arrangement of the PMs, two main categories can be identified:

- Surface-Mounted Permanent Magnets (surface magnets (SMs));
- Buried-Mounted Permanent Magnets (buried magnets (BMs)).

Rotors employing BMs provide improved mechanical robustness against centrifugal forces generated at high rotational speeds and eliminate the need for adhesive materials, which are typically required to bond the PMs to the rotor surfaces in SMs configurations.

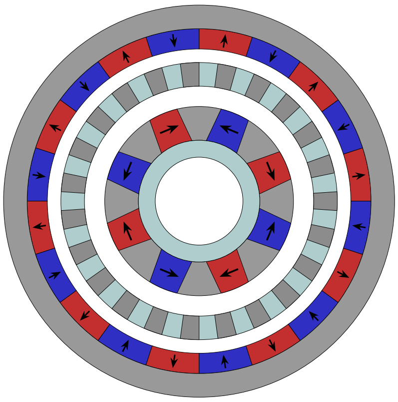

(a) Inner rotor with Buried-Mounted PMs, Outer rotor with Surface-Mounted PMs.

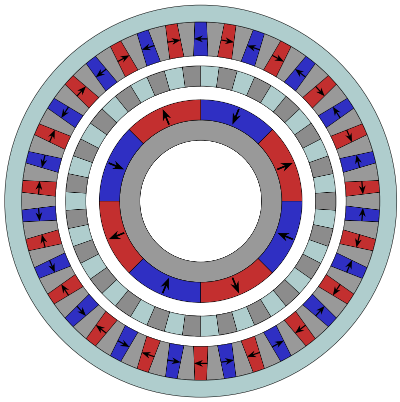

(b) Inner rotor with Surface-Mounted PMs, Outer rotor with Buried-Mounted PMs.

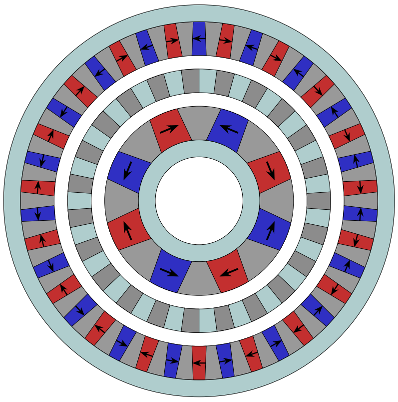

(c) Both rotors with Buried-Mounted PMs.

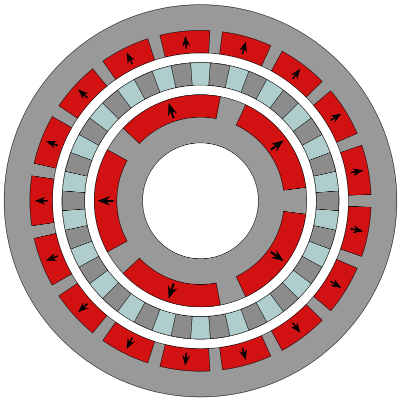

(d) All PMs with identical magnetization direction.

Figure 1.2: Examples of CMG topologies.

Regarding the magnetic field distribution, BMs generally exhibit alternating tangential magnetization directions. In contrast, SMs configurations allow a wider range of magnetization arrangements, including:

- Alternating radial magnetization (Figures 1.2a, 1.2b, 1.2c);
- Uniform radial magnetization (Figure 1.2d);
- Halbach arrays (Figure 1.4).

Figure 1.2d illustrates a CMG topology in which the PMs of both the Sun and Ring rotors are characterized by the same magnetization direction. For this reason, such a configuration is commonly referred to as a consequent-pole structure. In this topology, the ferromagnetic iron pieces between PMs are exploited to provide the magnetic flux path, allowing a reduction in the required volume of PMs without compromising too much torque density [5]. Consequently, this structure can reduce the amount of magnetic material and the overall manufacturing cost of the gear.

In the Halbach configuration, PMs with different magnetization directions are arranged in order to maximize the magnetic flux density on the side facing the ferromagnetic pole pieces while minimizing it on the opposite side. Figure 1.3 shows the magnetic field distribution of a Halbach array through a color map representation. It can be clearly observed that the magnetic field is strongly concentrated on one side of the array, whereas it becomes significantly weaker on the opposite side.

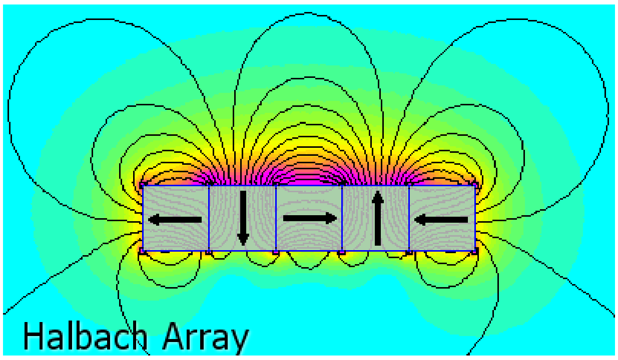

Figure 1.3: Example of Halbach array.

Examples of Halbach array CMGs are reported in Figure 1.4.

Figure 1.4a presents a CMG configuration in which both rotors employ Halbach arrays [6]. An example of a CMG combining unequal Halbach arrays with BMs, shown in Figure 1.4b, is proposed in [7]. Another variant, reported in Figure 1.4c, combines unequal Halbach arrays with a non-uniform air-gap [8]. These solutions enable an increase in the effective air-gap flux density and, consequently, an improvement in torque density.

Returning to the general classification of CMGs, the last criterion concerns the magnetic coupling direction, which can be either radial-flux or axial-flux. The configurations discussed so far belong to the radial-flux category, where the magnetic fields generated by the Sun and Ring rotors interact within a radial-tangential plane.

Examples of axial-flux CMGs are instead shown in Figure 1.5. In this case, the magnetic interaction between the Sun and Ring rotors occurs along the axial

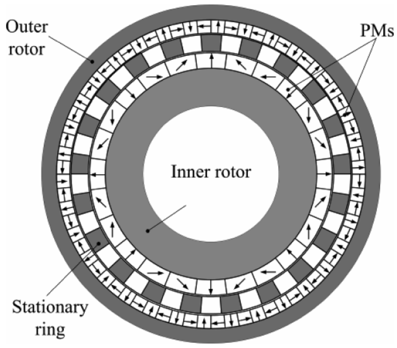

(a) Both rotors with Halbach arrays [6].

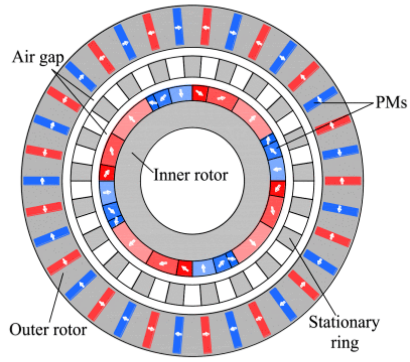

(b) Sun with unequal Halbach Array, Ring with BMs [7].

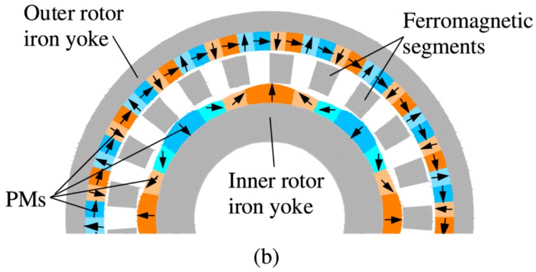

(c) Both rotors with Halbach array and non-uniform air-gap [8].

Figure 1.4: Examples of variations of Halbach arrays.

direction, since the magnetic fields are coupled through facing axial surfaces.

Despite the difference in flux direction, the fundamental operating principle of axial-flux CMGs remains identical to that of radial-flux configurations. Consequently, several methodologies adopted to improve the operational performance of radial-flux CMGs can also be applied to axial-flux solutions [1].

A quantitative comparison between radial-flux and axial-flux CMGs, based on coupled 3D finite element method (FEM) simulations of magnetic field distribution and mechanical motion, is presented in [9].

1.3 Examples of Industrial Applications

Examples of industrial applications of CMGs are presented in this section. In particular, applications concerning the replacement of conventional mechanical gearboxes, wind energy conversion systems, and industrial robotic arms are discussed.

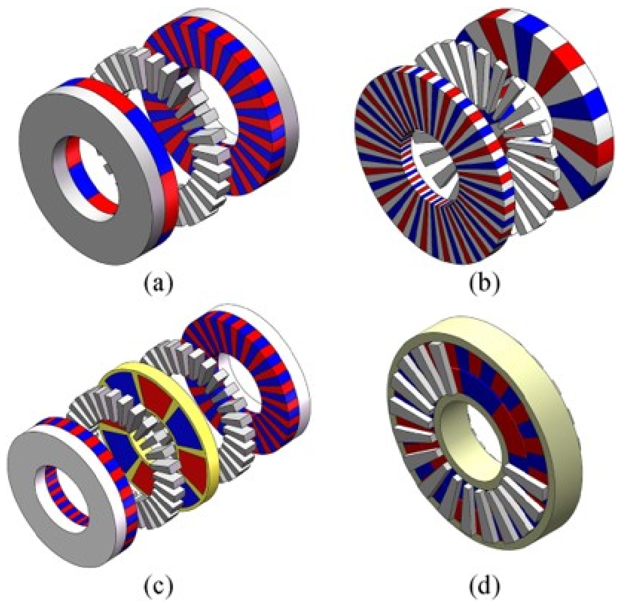

Figure 1.5: Examples of solutions of CMGs with axial-flux [1].

1.3.1 Magnetic Gearbox

By connecting multiple CMGs in series, each characterized by different transmission ratios, it is possible to realize a magnetic gearbox capable of replacing a conventional mechanical gearbox in all applications where the transmission ratio between a mechanical power source and a driven load must be modified [10].

Figure 1.6 shows the conceptual model of an equivalent six-speed magnetic gearbox, which is also capable of integrating the functions of a clutch and a torque limiter.

Depending on which component of the CMGs is displaced in order to achieve the transmission ratio variation, three different configurations can be identified:

- Translating Carrier;
- Translating Ring;
- Translating Sun;

Considering first the configuration with a translating Carrier, shown in Figure 1.7a, the axial displacement of the Carrier enables the switching between different CMGs. Since the number of ferromagnetic pole pieces remains constant for all the magnetic gears, different transmission ratios are obtained by varying the number of pole pairs of the Sun and Ring rotors.

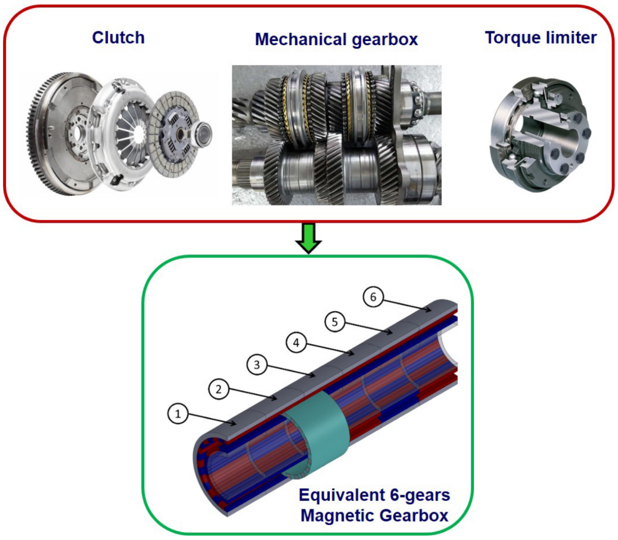

Figure 1.6: Equivalent Magnetic Gearbox solution [10].

Conversely, if the different CMGs share the same Ring rotor, as shown in Figure 1.7b, the PMs mounted on the Ring remain unchanged, while the ferromagnetic pole pieces of the Carriers and the PMs of the Sun rotors are modified. This configuration may provide an economic advantage compared to the previous solution, since only Sun rotors requires different PMs, whereas the variation of Carriers pole pieces involves lower costs than PMs.

A similar consideration applies to the third configuration, presented in Figure 1.7c, where the role previously played by the Ring rotor is instead assigned to the Sun rotor.

1.3.2 Wind Energy Harvesting

The application of CMGs has also attracted significant interest in the field of renewable energy systems. Their compact structure enables the replacement of conventional mechanical transmission systems employed for wind to electrical energy conversion.

In conventional wind power systems, the mechanical energy produced by the turbine is transferred through mechanical gear stages before being converted into electrical energy by the generator. The integration of turbines, mechanical gearboxes, and generators generally leads to bulky structures with increased installation volume, higher costs, and additional maintenance requirements.

Since the operational magnetic fields in CMGs are mainly distributed along the radial direction, the addition of an inner stator allows the direct integration of a PM electrical machine with the magnetic gear structure. By exploiting the

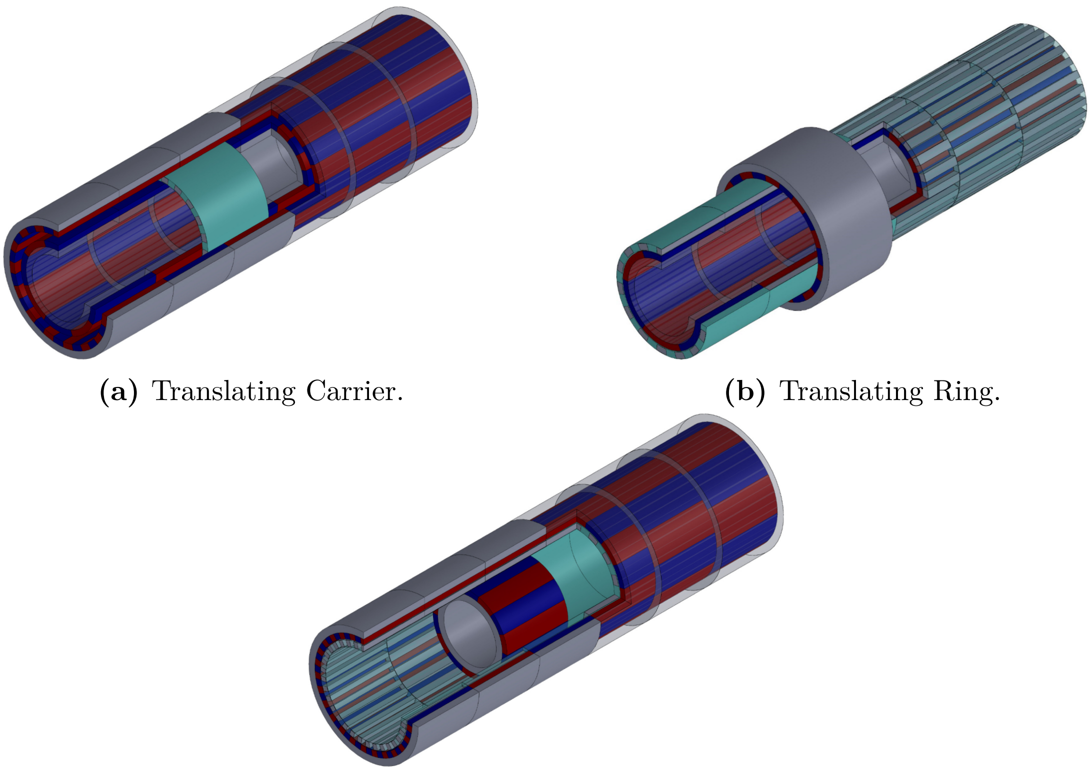

(a) Translating Carrier. **(b)** Translating Ring.

(c) Translating Sun.

Figure 1.7: Alternative configurations for transmission ratio variation in magnetic gearboxes [10].

double-rotor configuration and the coaxial magnetic gear principle, a PM generator capable of directly harvesting wind energy without mechanical transmission stages has been proposed in [11].

Figure 1.8 illustrates the structure of a CMG integrated with a three-phase generator. The wind turbine is mechanically connected to the outer rotor, characterized in this case by 17 pole pairs. Due to the low rotational speed imposed by the wind turbine, the outer rotor acts as the low-speed input stage of the system.

The magnetic gear constitutes the core of the device: the magnetic field generated by the outer rotor interacts with the 19 stationary ferromagnetic pole pieces, which modulate the field and drive the inner rotor, characterized by 2 pole pairs, at a significantly higher rotational speed and in the opposite direction.

The stator, carrying the three-phase windings, remains stationary. The magnetic flux produced by the high-speed inner rotor links the stator windings and induces the output voltage required for electrical power generation.

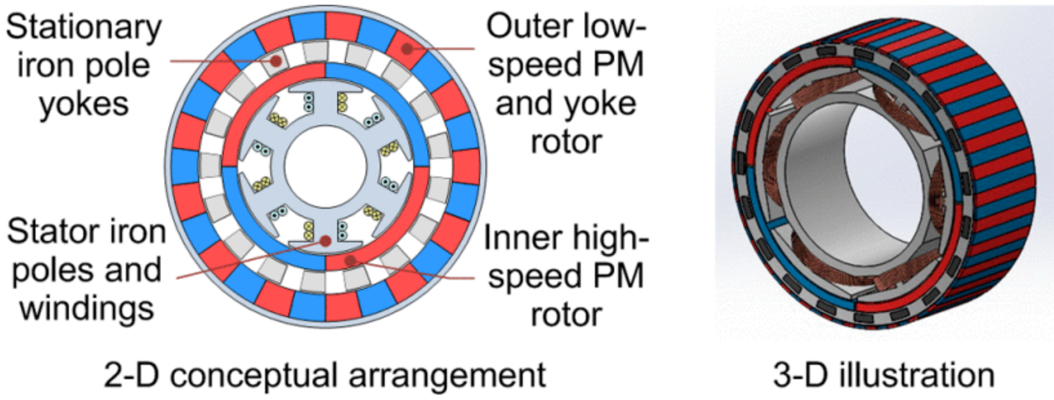

Figure 1.8: PM generator for wind energy harvesting [11].

1.3.3 Industrial Robot Arm Application

To overcome the limitations associated with conventional motor-gearbox assemblies, particularly the increase in installation volume and structural complexity, [12] proposes a magnetic geared permanent magnet synchronous motor (MG-PMSM) capable of achieving non-contact torque transmission through a single integrated drive device, while simultaneously providing the functionality of a mechanical reduction gear.

As shown in Figure 1.9, the MG-PMSM adopts a double-rotor structure composed of an inner and an outer rotor arranged along the same axis. Since the two rotors operate at different speeds and torque levels, the machine can be effectively employed in industrial robotic arm systems.

In particular, the external rotor, characterized by high torque output capability, can be directly connected to the robotic joint, thus simplifying the mechanical structure of the actuator. Compared with conventional systems combining mechanical gearboxes and electric motors, MG-PMSM solutions can provide significant improvements in terms of energy efficiency, compactness, and maintainability.

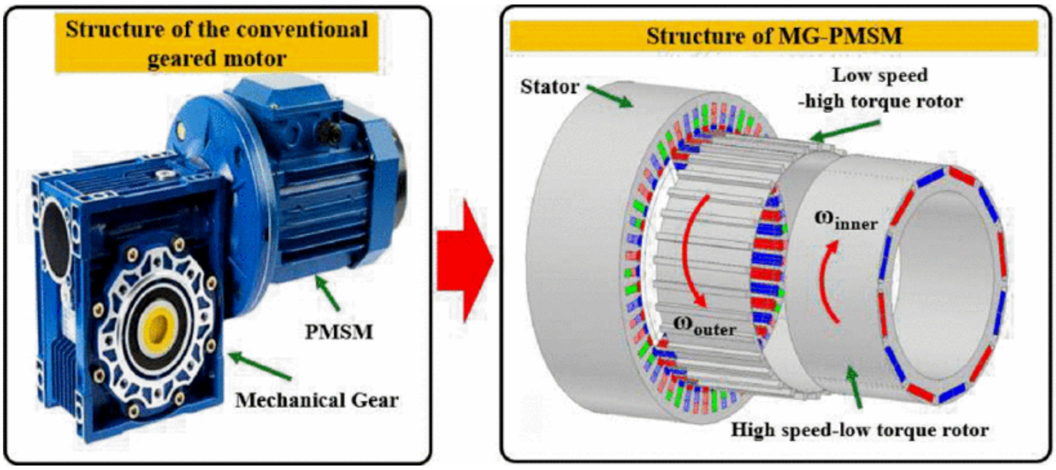

Figure 1.9: PMSM with conventional mechanical gearbox (left) and PMSM coupled with CMG (right) [12].

Chapter 2

Theory of CMG

This chapter presents the operating principles of a coaxial magnetic gear (CMG). After introducing the mechanisms responsible for torque transmission and the role of the ferromagnetic modulating elements, the analytical formulation of the device is discussed.

The mathematical model of the CMG is derived through the subdomain approach, in which the gear is divided into different regions characterized by distinct electromagnetic properties. The governing equations describing the magnetic field distribution within each region are then introduced and combined to obtain the overall analytical solution.

The chapter subsequently addresses the dynamic equations of the gear and the relationship between transmitted torque and load angle. Based on these formulations, the maximum transmissible torque is derived and discussed.

Finally, attention is focused on the loss mechanisms occurring in the permanent magnets. In particular, eddy-current losses are analyzed and a mitigation strategy based on magnet segmentation is presented. By dividing the permanent magnets into electrically insulated volumes, the circulation of induced currents can be significantly reduced, leading to lower power losses.

2.1 Reference systems

For the sake of clarity in the presentation of the concepts and in the description of the proposed figures, two reference systems will be adopted throughout the remainder of this work.

1. A Cartesian reference system (x, y, z) with origin located at the common geometric center of the three rotors, which are concentric elements. The z-axis coincides with the axis of rotation of the machine, while the x and y axes lie in the transversal plane.

2. A Cylindrical reference system (ρ, θ, z) defined with the same origin and axial direction as the Cartesian system. The radial coordinate ρ is measured from the rotation axis, the angular coordinate θ describes the circumferential position, and the z coordinate corresponds to the axial direction.

Angular velocities are defined according to the right-hand rule: when the rotation is counter-clockwise, as viewed from the positive z-axis, the angular velocity vector (ω) is directed along $+z$ and will be positive in sign $(\omega > 0)$.

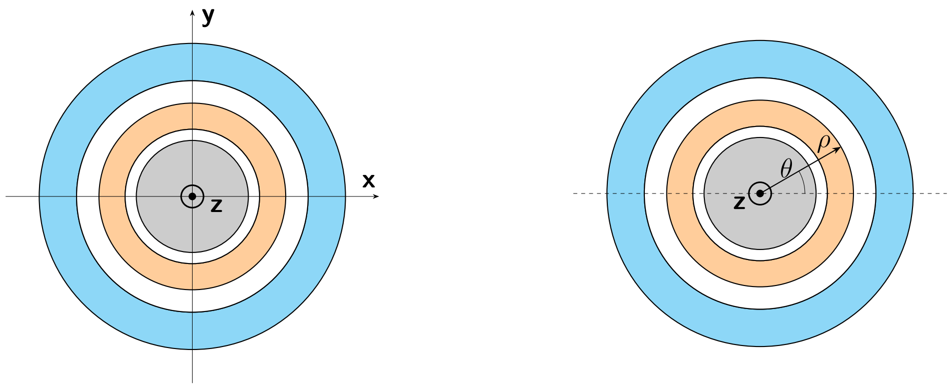

(a) **(b)**

Figure 2.1: Cartesian and Cylindrical reference systems used in this work.

2.2 Torque Generation in Electrical Machines

In the absence of physical contact between components, the torque in a rotating electrical machine is generated through the interaction between magnetic fields.

Figure 2.2a shows a simplified scheme of a two-pole machine. The north and south poles of the inner rotor are attracted, respectively, by the south and north poles of the outer rotor, resulting in a counter-clockwise torque.

If the two rotors have a different number of poles, no net torque is produced. For instance, as shown in Figure 2.2b, if the inner rotor has four poles and the outer rotor has two poles, two equal and opposite torques are generated, leading to a zero net torque.

More specifically, considering the poles N_1 and N_2 of the inner rotor, N_1 is repelled by the north pole and attracted by the south pole of the outer rotor, producing a counter-clockwise torque. Conversely, N_2 is also repelled by the north pole and attracted by the south pole, but due to its position, it generates a clockwise torque.

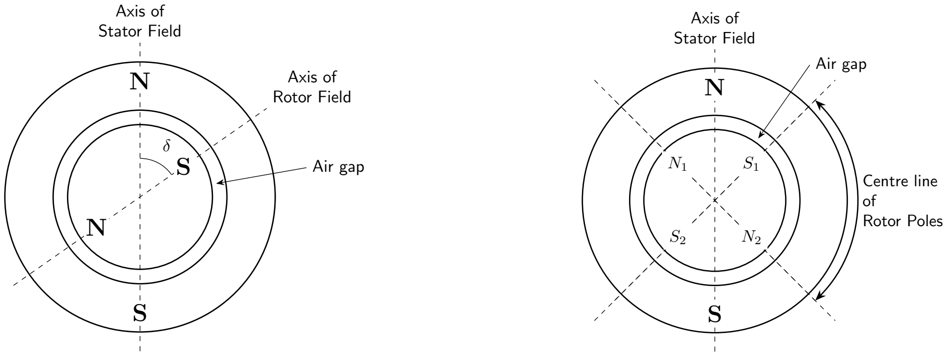

(a) Stator and rotor with equal number of poles.

(b) Stator and rotor with different number of poles.

Figure 2.2: Simplified machine schemes with different pole configurations [13].

A similar reasoning applies to the poles S_1 and S_2 of the inner rotor, resulting in an equivalent condition and confirming that the net torque is zero.

In conclusion, in order to obtain a non-zero net torque in a given direction, the two rotors must have the same number of poles.

2.3 Working Principle of CMG

Since the pole-pair numbers of the inner and outer rotors in CMGs are different, the operating principle is based on the flux modulation effect produced by the stationary ferromagnetic poles.

To better illustrate how the magnetic fields generated by the PM arrays of the inner and outer rotors interact, a linear representation of the CMG is adopted, as shown in Figure 2.3. This qualitative description is adapted from [13].

At the far left and far right, the PM arrays of the outer and inner rotors are shown, respectively. The magnets are arranged with alternating north and south magnetization directions. The black elements in the middle correspond to the ferromagnetic poles, while the modulated magnetic flux is shown between them and the inner rotor PMs.

For clarity, only the modulation of the magnetic field generated by the outer rotor is considered, while it interacts with the magnetic field of the inner rotor.

In Figure 2.3a, the ferromagnetic pole pieces are aligned with the PMs of the outer rotor characterized by a north-oriented magnetization. The effect is highlighted by the modulated flux distribution shown in the Figure. On the right side of the modulator, the magnetic flux exhibits the same orientation as that generated by the aligned outer rotor PMs, indicating that the ferromagnetic pole pieces provide a low-reluctance path for the magnetic field.

In Figure 2.3b, the ferromagnetic poles are aligned with the PMs of the outer rotor characterized by a south-oriented magnetization and consequently the modulated flux will have again the same orientation.

In Figure 2.3c, the ferromagnetic poles are unevenly aligned with respect to the PMs. Only the outermost PMs generate a modulated flux, creating one north and one south modulated fluxes, while the central ferromagnetic pole pieces, facing both north and south regions, do not contribute significantly to the flux.

The relative position between the outer rotor PMs and the ferromagnetic poles determines the modulation of the magnetic field and, therefore, the interaction between the two rotors.

2.4 Conventional Structure of CMG

The most common arrangement consists of mounting the PMs on the outer surface of the Sun rotor and on the inner surface of the Ring rotor, while the iron poles are inserted into the housings of the Carrier. This CMG topology (Figure 2.4) will be referred to as SM-CMG in the following chapters.

The structural analysis and the magnetic loss analysis presented in the following chapter are carried out considering this kinematic configuration:

- The Sun is connected to a high-speed shaft and is therefore referred to as the high-speed rotor;

- The Ring is connected to a low-speed shaft and is therefore referred to as the low-speed rotor;

- The Carrier is stationary.

2.5 Physical Quantities Used

In this section the main physical quantities used throughout the following chapters are introduced, namely the magnetic flux density $\mathbf{B}$, the magnetic field $\mathbf{H}$, the magnetization $\mathbf{M}$, the magnetic vector potential $\mathbf{A}$, the electric field $\mathbf{E}$, the electric scalar potential V, and the current density $\mathbf{J}$.

As shown in Figure 2.4 the magnetization vector is directed along the radial direction:

$$\mathbf{M} = M\mathbf{e}_\rho = \pm\frac{B_r}{\mu_0}\mathbf{e}_\rho. \tag{2.1}$$

where B_r is the magnitude of the residual flux density of the PMs.

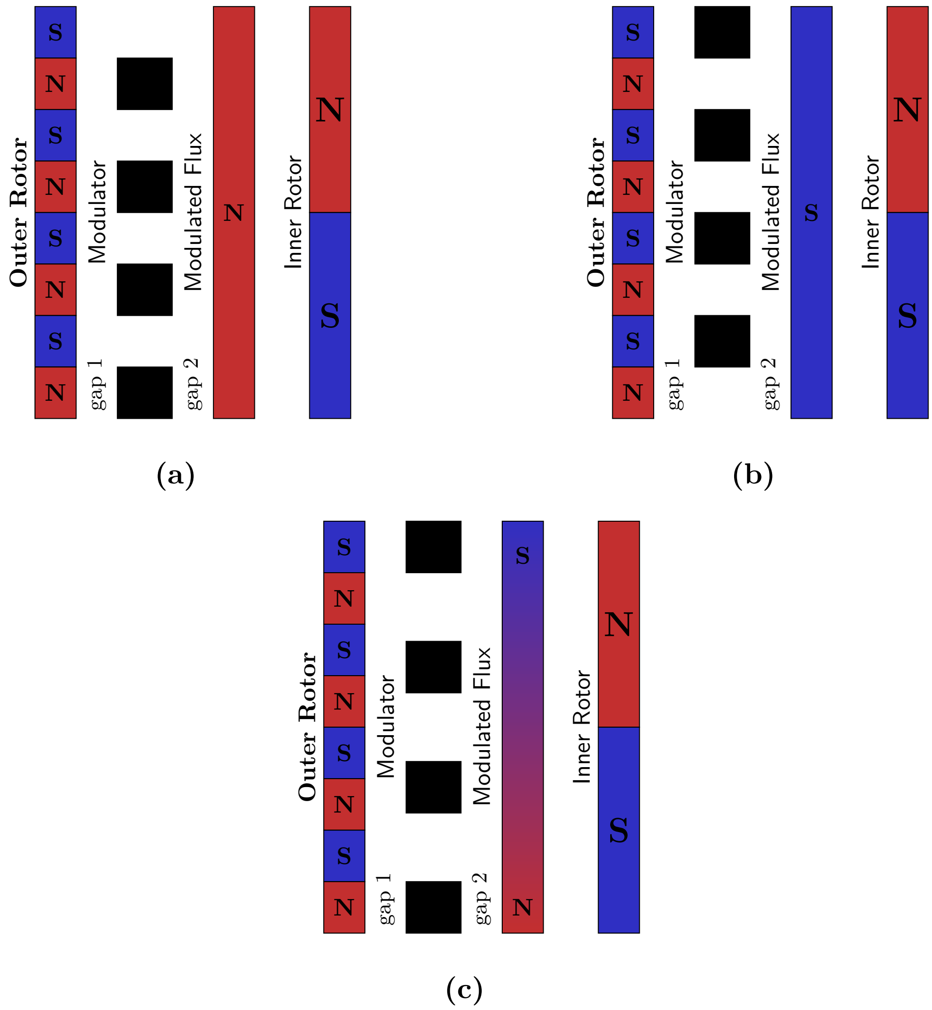

Figure 2.3: Linear model of CMG in different configurations [13].

The magnetic flux density can be expressed in terms of the magnetic vector potential as

$$\mathbf{B} = \nabla \times \mathbf{A}. \tag{2.2}$$

Moreover, the magnetic flux density, the magnetic field, and the magnetization are related by

$$\mathbf{B} = \mu_m \mathbf{H} + \mu_0 \mathbf{M}. \tag{2.3}$$

$$\mu_m = \mu_0 \mu_{m,rel}. \tag{2.4}$$

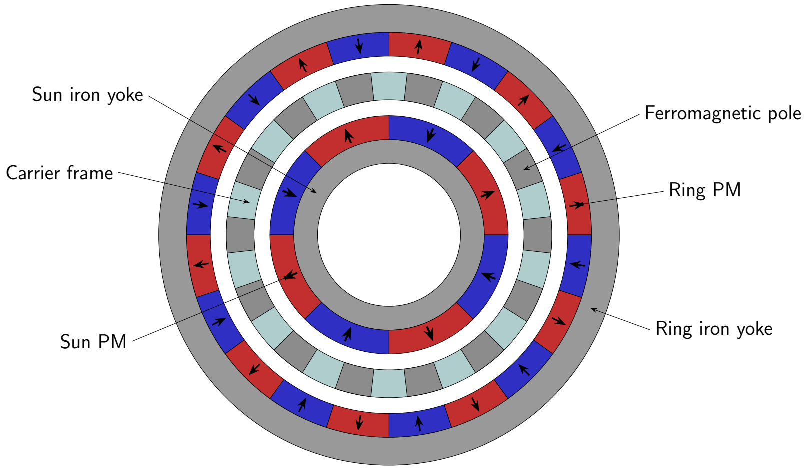

Figure 2.4: SM-CMG structure.

where μ_m is the magnetic permeability of the PMs and μ_0 is the permeability of free space. The quantity $\mu_{m,rel}$ denotes the relative magnetic permeability of the PMs, which relates the two parameters according to Equation (2.4).

The electric field and the electric scalar potential V are related by

$$\mathbf{E} = -\nabla V. \tag{2.5}$$

Current density vector and electric field are related by:

$$\mathbf{J} = \sigma \mathbf{E}. \tag{2.6}$$

Known also as Ohm's Law in local form. Where σ is the electrical conductivity.

2.6 Analytical Model

A qualitative description of the operating principle of CMGs was briefly introduced in Section 2.3. In this section, the principle of operation is explained in greater detail.

The first step consists in analytically describing the magnetic field produced by the arrays of PMs mounted on the Sun and Ring rotors. For this purpose, the magnetic flux density vector **B** will be considered.

This analysis leads to the introduction of the concept of *space harmonics* of the magnetic flux density. Subsequently, it will be shown how the modulation of these space harmonics, by the ferromagnetic poles of the Carrier, allows the magnetic interaction between the two rotors and therefore the transmission of torque.

2.6.1 Governing Equation

Following the derivation presented in [14], the governing equation is obtained by combining the Equations (2.2) and (2.6) with the following subset of Maxwell's equations:

$$\nabla \times \mathbf{H} = \mathbf{J} \tag{2.7}$$

$$\nabla \times \mathbf{E} = -\frac{\partial \mathbf{B}}{\partial t} \tag{2.8}$$

$$\nabla \cdot \mathbf{B} = 0 \tag{2.9}$$

Equations (2.7) to (2.9) represent, respectively, Ampère's law in magnetostatic form, Faraday's law of electromagnetic induction, and Gauss's law for magnetism, all expressed in their local differential form.

By combining Equations (2.5) and (2.8), the electric field can be expressed as

$$\mathbf{E} = -\frac{\partial \mathbf{A}}{\partial t} - \nabla V \tag{2.10}$$

Using Equations (2.2), (2.6), and (2.10), the current density becomes:

$$\mathbf{J} = -\sigma\frac{\partial \mathbf{A}}{\partial t} - \sigma\nabla V \tag{2.11}$$

The first term on the right-hand side represents the internally generated eddy current density, while the second term corresponds to the externally impressed source current density [15].

Then, by substituting Equations (2.2), (2.3), and (2.11) into Equation (2.7), the following formulation in terms of the magnetic vector potential is obtained:

$$\nabla \times (\nabla \times \mathbf{A}) = -\sigma\mu_m\frac{\partial \mathbf{A}}{\partial t} - \sigma\mu_m\nabla V + \mu_0\nabla \times \mathbf{M} \tag{2.12}$$

Finally using Equation (2.2) it is possible to evaluate **B**.

2.6.2 Subdomain Model

The adopted solution strategy for Equation (2.12) consists in first evaluating the magnetic vector potential **A** in the space between the Sun and the Ring rotors. This region is divided into several subdomains, as illustrated in Figure 2.5.

Regions I and V correspond to the volumes occupied by the PMs. Regions II, III, and IV represent respectively the inner air-gap, the carrier frame (region without ferromagnetic poles), and the outer air-gap.

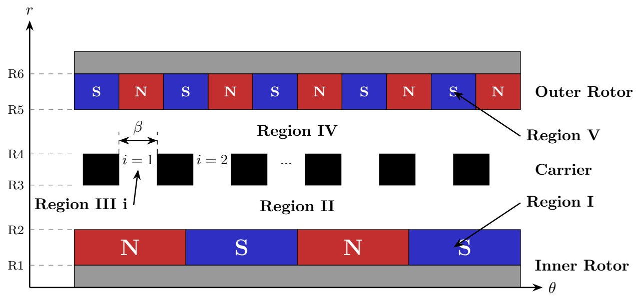

Figure 2.5: Scheme of CMG divided in subdomains.

The analytical modelling of CMGs based on the subdomain approach has been extensively investigated in the literature, as reported for instance in [16] and [17]. In [5], the same subdomain method is applied to a consequent-pole rotor configuration of a SM-CMG.

In order to simplify the analytical formulation, the following assumptions are introduced:

- The magnetic permeability of the ferromagnetic material is assumed to be infinite $\mu_{Fe} = \infty$ (the magnetic field in the iron vanishes);
- Axial end effects of the magnetic field are neglected;
- The relative magnetic permeability of the PMs is assumed to be $\mu_{m,rel} \approx 1$;
- The considered field quantities have the following non-zero components:

$$A = [0,0,A_z], \quad J = [0,0,J_z], \quad M = [M_\rho,0,0], \quad B = [B_\rho, B_\theta,0].$$

In the present analysis, a magneto-static approximation is adopted. Under this assumption, the time derivative term $\partial\mathbf{A}/\partial t$ vanishes and the electric scalar potential gradient term ∇V can be neglected as no external current sources are present. Consequently, Equation (2.12) reduces to:

$$\nabla \times (\nabla \times \mathbf{A}) = \mu_0 \nabla \times \mathbf{M}. \tag{2.13}$$

Furthermore, by adopting the Coulomb gauge condition $\nabla \cdot \mathbf{A} = 0$, the vector identity

$$\nabla \times (\nabla \times \mathbf{A}) = \nabla(\nabla \cdot \mathbf{A}) - \nabla^2 \mathbf{A} \tag{2.14}$$

simplifies to:

$$\nabla \times (\nabla \times \mathbf{A}) = -\nabla^2 \mathbf{A}. \tag{2.15}$$

With these assumptions, the governing equation takes two different forms depending on the region under consideration:

$$\nabla^2 \mathbf{A}_i = 0 \qquad i = \text{II, III, IV} \tag{2.16}$$

$$\nabla^2 \mathbf{A}_i = -\mu_0 \nabla \times \mathbf{M} \qquad i = \text{I, V} \tag{2.17}$$

The difference in the right-hand side of these two equations is due to the presence of permanent magnets in regions I and V, which act as magnetic sources through their magnetization $\mathbf{M}$. Equation (2.16) represents Laplace's equation, which applies to the non-magnetized regions (II, III, IV), while Equation (2.17) corresponds to Poisson's equation in the magnetized regions (I, V).

In order to derive an analytical solution of Equations (2.16) and (2.17) the cylindrical reference system introduced in Section 2.1 is adopted. The magnetic vector potential is therefore expressed in two-dimensional polar coordinates as $\mathbf{A}(\rho, \theta)$ [5].

The Equations (2.16) and (2.17) then can be written as:

$$\nabla^2 A(\rho, \theta) = \frac{\partial^2 A}{\partial \rho^2} + \frac{1}{\rho}\frac{\partial A}{\partial \rho} + \frac{1}{\rho^2}\frac{\partial^2 A}{\partial \theta^2} = 0 \tag{2.18}$$

$$\nabla^2 A(\rho, \theta) = \frac{\partial^2 A}{\partial \rho^2} + \frac{1}{\rho}\frac{\partial A}{\partial \rho} + \frac{1}{\rho^2}\frac{\partial^2 A}{\partial \theta^2} = \frac{\mu_0}{\rho}\left(\frac{\partial M_\rho}{\partial \theta} - M_\theta\right) \tag{2.19}$$

Where in Equation (2.19) the magnetization vector $\mathbf{M}$ is represented by its radial (M_ρ) and tangential (M_θ) components.

2.6.3 Example of Solution: Magnetic Field Distribution in Regions I, II

Within each subdomain, the governing partial differential equations Equations (2.18 and 2.19) are solved by means of the separation of variables technique.

Only the solutions for the magnetic vector potential in selected regions are reported. In particular, the focus is placed on the PMs region of the Sun (Region I) and on the air-gap between the Sun and Carrier (Region II).

Following the formulation proposed in [16], the general solution for the z-component of the magnetic vector potential in Region I and II is expressed as an infinite Fourier series composed of spatial harmonics:

$$
\begin{cases}
A_I(r,\theta) = \sum_{n=1}^{\infty} \Big(A_{I,n} r^n + B_{I,n} r^{-n} + W_{I,n}(r)\cos(n\psi_i) \Big) \cos(n\theta) \\
\qquad\qquad + \sum_{n=1}^{\infty} \Big(C_{I,n} r^n + D_{I,n} r^{-n} + W_{I,n}(r)\sin(n\psi_i) \Big) \sin(n\theta) \\
A_{II}(r,\theta) = \sum_{n=1}^{\infty} \Big(A_{II,n} r^n + B_{II,n} r^{-n} \Big) \cos(n\theta) \\
\qquad\qquad + \sum_{n=1}^{\infty} \Big(C_{II,n} r^n + D_{II,n} r^{-n} \Big) \sin(n\theta)
\end{cases}
\tag{2.20}
$$

where $W_{I,n}(r)$ coefficient is defined as:

$$
W_{I,n}(r) = \begin{cases}
4B_r p_i r/(\pi(1-n^2)) & \text{if } n = jp_i,\ j = 1,3,5,\dots \\
2B_r r \ln r/\pi & \text{else if } n = p_i = 1 \\
0 & \text{otherwise}
\end{cases}
\tag{2.21}
$$

In both Equations in (2.20) the coefficients $A_{I/II,n}, B_{I/II,n}, C_{I/II,n}, D_{I/II,n}$ are determined by enforcing boundary conditions, specifically the continuity of the tangential magnetic field and the normal flux density at the interfaces between adjacent subdomains.

In Equation (2.21) B_r is the residual flux of PMs of the Sun and p_i is the pole-pairs number of the Sun; ϕ_i and ϕ_o are respectively the initial angles of the inner rotor and outer rotor; β is the angle of the slot between modulation pole-pieces. In both the above equations n is the order of the Fourier's series.

Once the potentials $A_{\mathrm{I/II}}$ is established, the radial and tangential components of the magnetic flux density vector $\mathbf{B}$ are derived using the curl operator (2.2) in polar coordinates:

$$
B_r^{\mathrm{I/II}} = \frac{1}{r}\frac{\partial A_z^{\mathrm{I/II}}}{\partial \theta} \quad ; \quad B_\theta^{\mathrm{I/II}} = -\frac{\partial A_z^{\mathrm{I/II}}}{\partial r}
\tag{2.22}
$$

The analytical solutions derived in (2.22) are validated by means of a FEM model. Figure 2.6 shows the radial and tangential components of the magnetic flux density in the inner air-gap between the sun and the carrier rotors.

It can be observed that, for both components, the FEM results closely overlap with the analytical solutions.

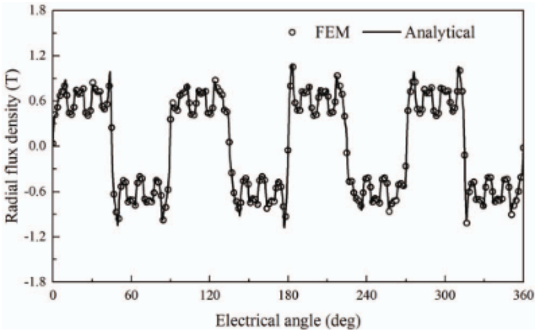

(a) Inner air-gap radial flux density.

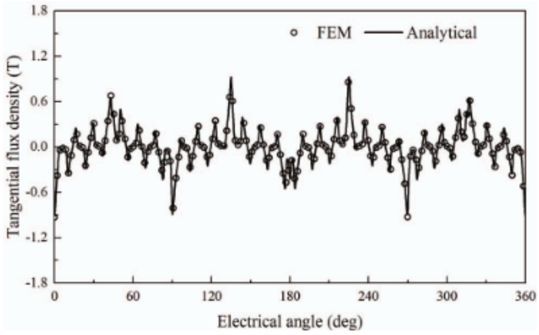

(b) Inner air-gap tangential flux density.

Figure 2.6: FEM vs. analytical solutions for magnetic flux distribution [16].

2.7 Condition for Torque Transmission

Let p_s and p_r denote the number of pole pairs of either the inner rotor or the outer rotor, and n_s the number of ferromagnetic pole pieces in the carrier. The number of pole pairs associated with the resulting harmonics is given by:

$$\begin{aligned} p_{m,k} &= |mp + kn_s| \\ m &= 1, 3, 5, \ldots, \infty \\ k &= 0, \pm 1, \pm 2, \pm 3, \ldots, \pm\infty \end{aligned} \tag{2.23}$$

It is important to notice that the velocity of rotation of the harmonics is different from the rotational velocity of the rotor that generated them. This is caused by the presence of the iron poles n_s so it must be $k \neq 0$. As a consequence, in order to transmit torque from Sun to Ring at different speed, the number of PMs pole pairs of the Ring must be equal to the number of pole pairs of a space harmonics generated from the Sun. For both rotors the largest of these harmonics that they interact with is with $m = 1, k = -1$ [3].

Figures 2.7 and 2.8 show the spectra of the spatial harmonics of the radial component of the magnetic flux density in the outer and inner air-gaps, respectively.

The example considered refers to a CMG with $p_s = 4$, $p_r = 22$, and $n_s = 26$. It can be observed from Figure 2.7 that the dominant space harmonic generated by the Sun (excluding the $k = 0$ component) in the outer air-gap adjacent to the Ring corresponds to $m = 1$, $k = -1$, yielding $p_{1,-1} = 22 = p_r$.

Similarly, from Figure 2.8, the dominant space harmonic generated by the Ring in the inner air-gap adjacent to the Sun is associated with $m = 1$, $k = -1$, yielding $p_{1,-1} = 4 = p_s$.

This demonstrates that the modulation effect enables each rotor to interact with the magnetic field produced by the other. In general, by applying Equation (2.23)

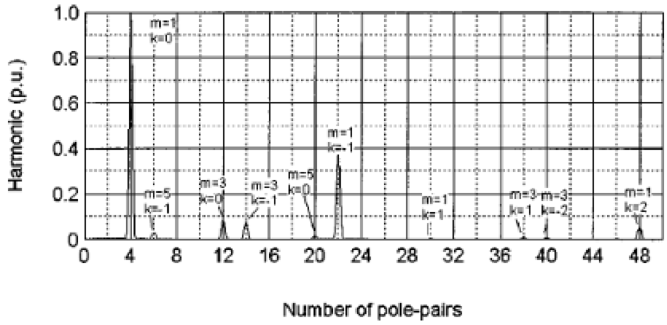

Figure 2.7: Space harmonic of radial flux density generated by the sun acting in the outer air-gap [3].

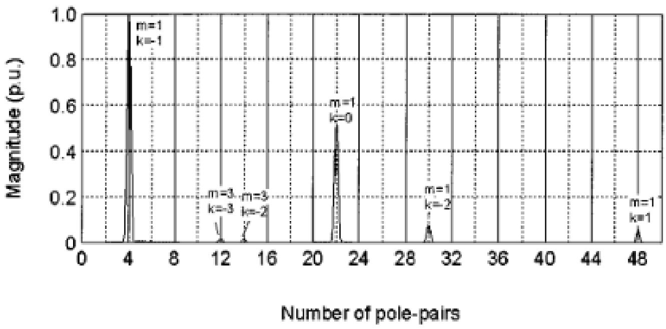

Figure 2.8: Space harmonic of radial flux density generated by the ring acting in the inner air-gap [3].

to both rotors, the following relationships are obtained:

$$\begin{gathered} p_r = |p_s - n_s| \\ (m = 1, k = -1) \end{gathered} \tag{2.24}$$

$$\begin{gathered} p_s = |p_r - n_s| \\ (m = 1, k = -1) \end{gathered} \tag{2.25}$$

Equation (2.24) indicates that, among the harmonics generated by the Sun, the dominant one interacting with the Ring (i.e., present in the outer air-gap) has a number of pole pairs equal to the number of pole pairs of the Ring.

Conversely, Equation (2.25) shows that the dominant harmonic generated by the Ring and interacting with the Sun (i.e., present in the inner air-gap) has a number of pole pairs equal to number of pole pairs of the Sun.

Solving Equations (2.24), (2.25) with the conditions $0 < p_r < n_s$ and $0 < p_s < n_s$ the condition for torque transmission in a CMG is given by:

$$p_r + p_s = n_s \tag{2.26}$$

2.8 Dynamic Equations

In reference to [18], the equations of motion of the CMG can be derived by considering the free-body diagrams of its individual components. Figure 2.9 shows the free-body diagram of the entire CMG. The external torques (T_s, T_c, T_r) are assumed to be in the same direction of the corresponding angular velocities of the rotors, here denoted as $\dot{\vartheta}_s$, $\dot{\vartheta}_c$, and $\dot{\vartheta}_r$.

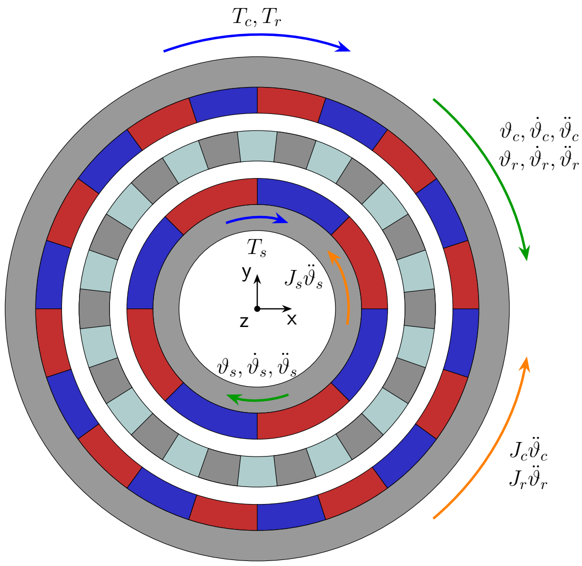

Figure 2.9: Free-body diagram of the CMG [18].

By separating the global free-body diagram into three distinct diagrams, each corresponding to one rotor (see Figure 2.4), the equations of motion can be written as:

$$\begin{cases} J_s\ddot{\vartheta}_s = T_s - T_{MG_{sc}} \\ J_c\ddot{\vartheta}_c = T_c + T_{MG_{sc}} + T_{MG_{cr}} \\ J_r\ddot{\vartheta}_r = T_r - T_{MG_{cr}} \end{cases} \tag{2.27}$$

These equations can be rearranged in matrix form as:

$$\begin{bmatrix} J_s & 0 & 0 \\ 0 & J_c & 0 \\ 0 & 0 & J_r \end{bmatrix} \begin{Bmatrix} \ddot{\vartheta}_s \\ \ddot{\vartheta}_c \\ \ddot{\vartheta}_r \end{Bmatrix} = \begin{Bmatrix} T_s \\ T_c \\ T_r \end{Bmatrix} + \begin{Bmatrix} -T_{MG_{sc}} \\ T_{MG_{sc}} + T_{MG_{cr}} \\ -T_{MG_{cr}} \end{Bmatrix} \tag{2.28}$$

The terms T_s, T_c, and T_r represent the external torques acting on the sun, carrier, and ring, respectively. The angular position, velocity, and acceleration of each rotor are denoted by ϑ, $\dot{\vartheta}$, and $\ddot{\vartheta}$.

The torques $T_{MG_{sc}}$ and $T_{MG_{cr}}$ represent the magnetic torques generated by the interaction of the magnetic flux between the Sun and Carrier, and between the Carrier and Ring, respectively. Finally, the parameters J_s, J_c, and J_r denote the moments of inertia of the three rotors.

Considering the configuration described in Section 2.4, where the Carrier is assumed to be stationary, T_s can be interpreted as the input torque provided by a driving motor, while T_r represents the load torque applied to the Ring.

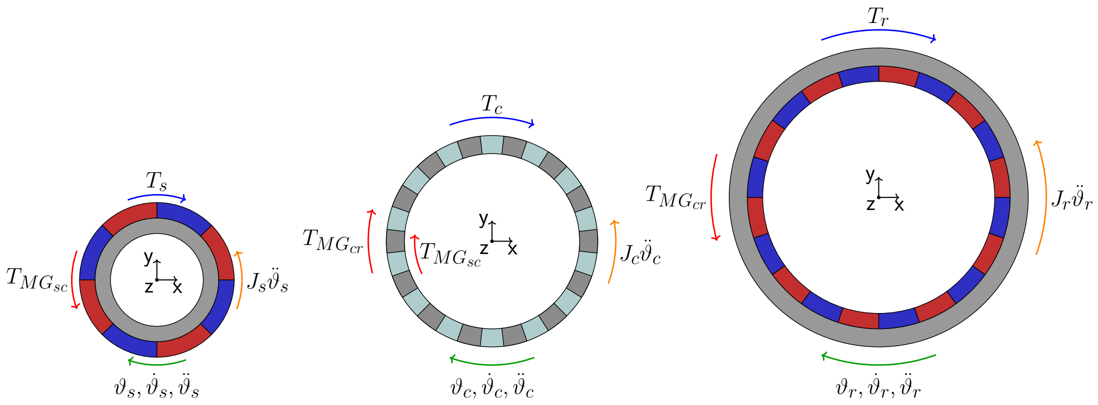

Figure 2.10: Free body diagram of Sun (left), Carrier (middle) and Ring (right) rotors [18].

2.8.1 Gear Ratio Definition

The similarities between mechanical and magnetic gears extend beyond the nomenclature of their components (e.g., Sun and Ring rotors) and can also be observed in the definition of the gear ratio.

As previously discussed, torque transmission in CMGs does not occur through mechanical contact between teeth, but rather through the interaction of magnetic fluxes.

Defining the angular velocities as ω_s, ω_c, and ω_r, and considering the case of a stationary Carrier ($\omega_c = 0$), the gear ratio can be expressed using the Willis equation [19] as:

$$\begin{cases} \tau_{s,r_{mag}} = \dfrac{\omega_s - \omega_c}{\omega_r - \omega_c} = \dfrac{\omega_s}{\omega_r} = -\dfrac{p_r}{p_s} < 0 \\ \tau_{s,r_{mech}} = \dfrac{\omega_s - \omega_c}{\omega_r - \omega_c} = \dfrac{\omega_s}{\omega_r} = \dfrac{Z_p}{Z_s} \cdot \dfrac{Z_r}{Z_p} = -\dfrac{Z_r}{Z_s} < 0 \end{cases} \tag{2.29}$$

where $\tau_{s,r_{mag}}$ denotes the gear ratio of the CMG, while $\tau_{s,r_{mech}}$ represents the gear ratio of a mechanical planetary gear.

As introduced in Section 2.7, p_s and p_r denote the number of pole pairs of the Sun and Ring rotors, respectively. In contrast, the mechanical counterpart is characterized by the number of teeth of the Sun, Planets, and Ring gears, denoted as Z_s, Z_p, and Z_r.

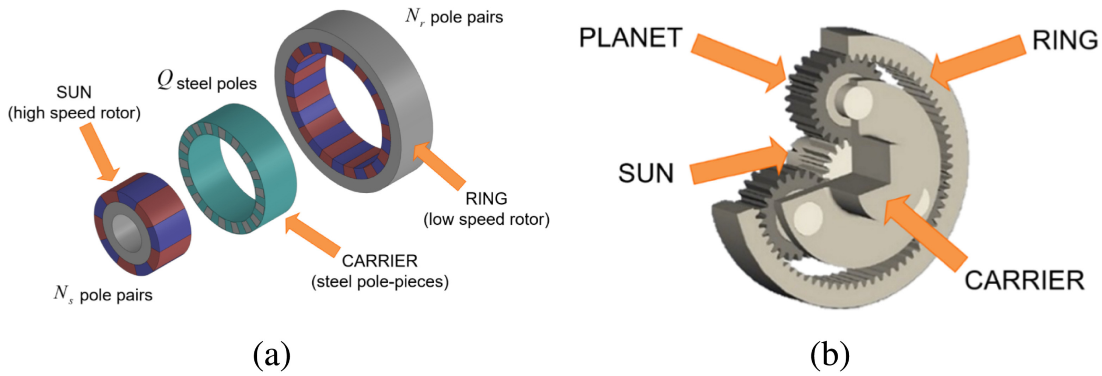

Figure 2.11: Exploded view of the SM-CMG and corresponding elements of a mechanical planetary gear [10].

In a mechanical planetary gear, the planet gears are responsible for transmitting torque from the Sun to the Ring. In a CMG, this role is fulfilled by the Carrier and its ferromagnetic pole pieces, which, through the flux modulation effect described in Section 2.7, enable torque transmission between the rotors.

2.8.2 Torque-Angle Characteristic

Assuming a fixed Carrier and neglecting both losses and cogging torque, the torque T_m transmitted by the CMG (evaluated at the Ring rotor) can be expressed as [20]:

$$T_m = T_M \sin \theta_e, \tag{2.30}$$

where T_M denotes the maximum transmissible torque at the Ring, and θ_e is the load angle, defined as

$$\theta_e = p_s\theta_s + p_r\theta_r - n_s\theta_c. \tag{2.31}$$

Under normal operating conditions, the transmitted torque T_m remains below the limit torque T_M, corresponding to $|\theta_e| < \frac{\pi}{2}$. When this condition is violated, i.e., when $T_m > T_M$, magnetic synchronization is lost due to the misalignment of the magnetic fields. As a consequence, a slipping condition occurs between the interacting rotors, and the Ring rotor motion becomes dependent on the external load characteristics.

In order to determine the limit torque of a CMG as a function of the load angle, a numerical approach can be adopted as proposed in [21]. In this method, one of the two moving rotors (e.g., the outer rotor) is kept fixed, while the inner rotor is incrementally rotated. At each angular position, the torque is evaluated using the Maxwell stress tensor formulation [22].

The electromagnetic torque (EMT) acting on the inner and outer air-gaps can be expressed as:

$$T_i = \frac{l\rho_i^2}{\mu_0} \int_0^{2\pi} B_{\rho_i}(\rho_i, \theta)\, B_{\theta_i}(\rho_i, \theta)\, d\theta \tag{2.32}$$

$$T_o = \frac{l\rho_o^2}{\mu_0} \int_0^{2\pi} B_{\rho_o}(\rho_o, \theta)\, B_{\theta_o}(\rho_o, \theta)\, d\theta \tag{2.33}$$

The parameter l denotes the axial length of the PMs, while ρ_i and ρ_o are the radii of the circular integration paths corresponding to the inner and outer air-gaps. The quantities $B_\rho(\rho, \theta)$ and $B_\theta(\rho, \theta)$ denote the radial and tangential components of the magnetic flux density evaluated along these paths.

The results obtained from FEM simulations can be post-processed to evaluate the torque as a function of the relative angular displacement between the rotors. A typical torque–angle characteristic is shown in Figure 2.12, from which the limit torque and the stable operating region can be identified.

2.9 Magnets Losses in CMGs

The operational efficiency of CMGs is significantly influenced by the dissipation of energy within their active components. As investigated in [23], magnetic losses in these structures arise from the complex relative motion between PMs and ferromagnetic modulator poles. These losses are primarily categorized into hysteresis and eddy currents losses. Eddy currents are closed-loop electric currents induced within conductive materials due to time-varying magnetic fields or relative motion between a conductor and a magnetic field source.

According to Faraday's law of induction (2.8), a variation of magnetic flux density through a conductive region generates an electromotive force that drives circulating currents inside the material. By Lenz's law, the magnetic field produced by these currents opposes the variation of magnetic flux that generated them.

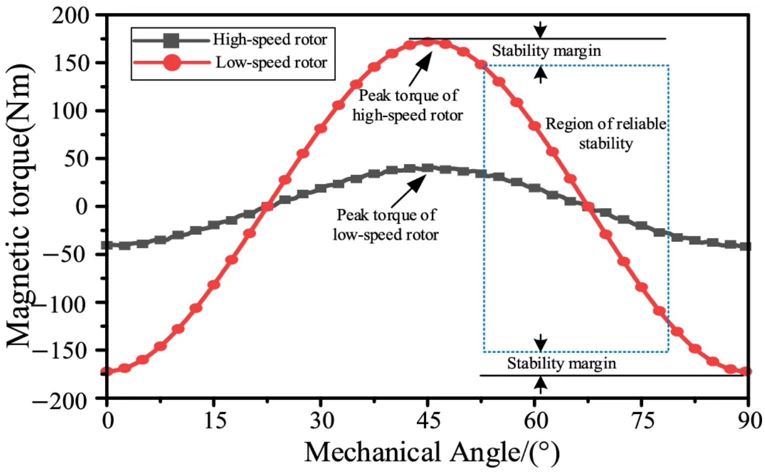

Figure 2.12: Torque as a function of the load angle [21].

Within a CMG, the relative motion between the rotating PMs and the ferromagnetic pole pieces continuously modifies the magnetic field distribution inside the magnets. Consequently, local variations of magnetic flux density induce circulating currents inside the conductive volume of the PMs. These currents form conductive loops whose magnitude depends on the magnetic field strength, the variation rate of the magnetic flux, the conductive path area, and the electrical conductivity of the material.

The fundamental mechanism of eddy currents dissipation is governed by the **J** term introduced in Equation (2.11). In a conductive medium with volume V, the instantaneous power loss P_{eddy} is defined by the volume integral of the local power density, corresponding to the scalar product between the current density **J** and the electric field **E**:

$$P_{eddy} = \int_V (\mathbf{J} \cdot \mathbf{E})\, dV \tag{2.34}$$

Assuming the material to be isotropic and characterized by a constant electrical conductivity σ, Ohm's law in its local form (2.6) can be applied. The total eddy current losses can therefore be rewritten as:

$$P_{eddy} = \int_V \frac{|\mathbf{J}|^2}{\sigma}\, dV \tag{2.35}$$

This expression represents the standard formulation adopted in FEM post-processing for the evaluation of eddy current losses in conductive components.

2.9.1 Computational Methods and Mitigation through Segmentation

The accurate estimation of these losses is computationally demanding due to the high-frequency harmonics generated by the magnetic flux modulation process. According to [24], although two-dimensional and three-dimensional FEM simulations remain the benchmark in terms of accuracy, hybrid approaches combining analytical formulations with numerical methods are increasingly adopted in order to improve computational efficiency.

To reduce losses, structural modifications such as magnet segmentation are commonly introduced. The underlying principle, described in [25], consists in increasing the equivalent electrical resistance of the eddy current paths by subdividing the PMs into smaller insulated segments. This strategy reduces the available conductive loop area, thereby significantly limiting the magnitude of the induced current density $\mathbf{J}$ and, consequently, the associated losses.

However, the effectiveness of segmentation strongly depends on the harmonic content of the machine and on the geometrical arrangement of the magnetic structure. An improper segmentation strategy may lead to unexpected increases in losses or to additional manufacturing complexity.

Chapter 3

Model CMG with BM

This chapter provides a detailed description of the geometry modelling procedure implemented in SIMULIA Opera 3D Modeller for the electromagnetic simulations carried out in this work.

Two different configurations are investigated. The first one considers non-segmented PMs, while the second adopts segmented PMs, including both axial segmentation of the Sun rotor magnets and radial segmentation of the Ring rotor magnets.

The final part of the chapter is dedicated to the simulation settings and numerical procedures adopted in the FEM analyses. Two different simulation are considered: the first is aimed at determining the maximum transmissible torque of the proposed magnetic gear, whereas the second focuses on the evaluation of eddy-current losses within the PMs during operation.

3.1 Structure of BM-CMG

One drawback of the surface-mounted configuration is related to the mechanical retention of the PMs. In high-speed applications, the magnets mounted on the Sun rotor are subjected to significant centrifugal forces. Consequently,mechanical solutions, such as adhesive bonding or mechanical fastening elements, are typically required to ensure the structural integrity of the assembly.

In order to overcome these limitations as explained in Section 1.2, the alternative configuration named BM-CMG is considered in this work.

The operating principle remains unchanged, as described in Chapter 2: the main space harmonic of magnetic flux density generated by the sun is modulated through the iron poles of the carrier. It then interacts with the the main space harmonic of magnetic flux density of the ring to produce torque transfer.

3.2 Model description

In Table 3.1 are listed the parameters used to model the geometry in SIMULIA Opera 3D Modeller.

Parameter	Symbol	Value	Unit
sun pole-pairs	p_S	4	-
ring pole-pairs	p_R	19	-
carrier iron pairs	n_s	23	-
gear ratio	τ	-4.75	-
sun inner radius	R1	40	mm
sun outer radius	R2	60	mm
carrier inner radius	R3	61	mm
carrier outer radius	R4	71	mm
ring inner radius	R5	72	mm
ring outer radius	R6	90	mm
gear axial length	h	30	mm
inner gap	g_1	1.0	mm
outer gap	g_2	1.0	mm
sun magnets inner wedge factor	α_S	1.4	-
sun magnets outer wedge factor	β_S	1.1	-
ring magnets inner wedge factor	α_R	1.0	-
ring magnets outer wedge factor	β_R	1.0	-

Table 3.1: Parameters of BM-CMG model.

Figure 3.1 shows the final geometry of the inner rotor. The PMs (white blocks) are surrounded by ferromagnetic yokes (grey regions).

The parameter H_{mag} is the average thickness of the permanent magnets calculated as:

$$H_{mag} = (R_{int} + R_{ext})/2 \cdot \Delta\theta/3; \tag{3.1}$$

$$\Delta\theta = 2 \cdot \pi/(2 \cdot p); \tag{3.2}$$

where $\Delta\theta$ is the angular amplitude calculated for both rotors using the different pole-pairs (p_s or p_r) value assigned to them. The α and β factors correspond to the inner and outer wedge factors of the PM.

A similar approach is adopted to model the outer rotor, using the corresponding geometric parameters, in particular the wedge factors reported in Table 3.1.

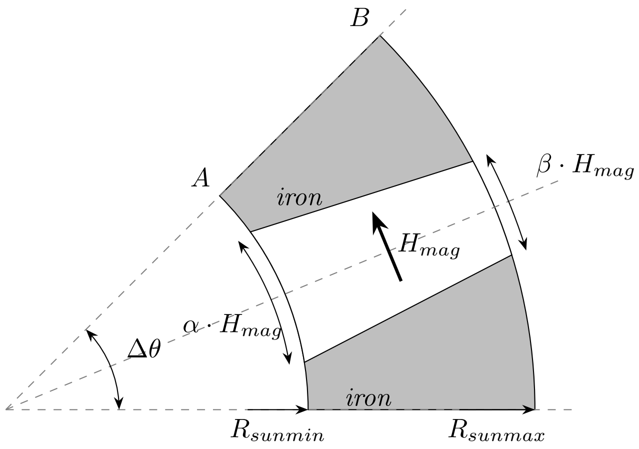

Figure 3.1: Inner rotor geometry in the BM-CMG model.

In this configuration, the magnetization direction is tangential. Along the circumference of each rotor, the magnets are arranged with alternating magnetization directions.

Figure 3.2 illustrates the complete model, where the magnetization vectors of each magnet are explicitly shown.

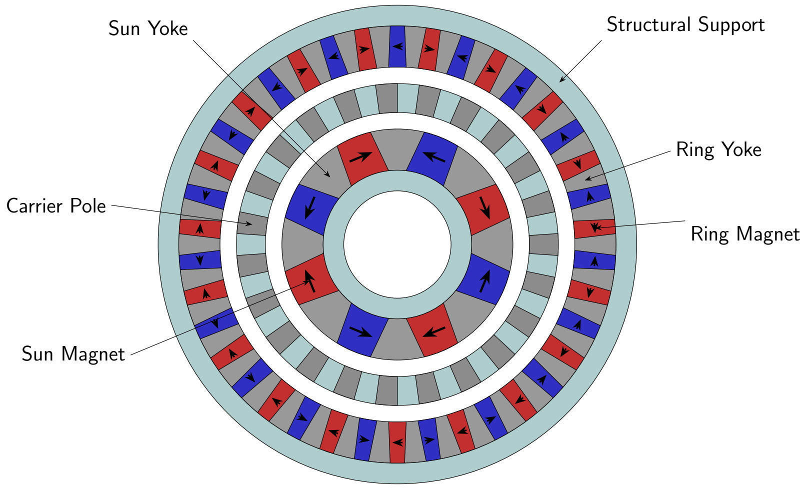

Figure 3.2: Model structure of BM-CMG.

The model was first built and simulated using non-segmented PMs. It was then modified to include both radial and tangential segmentations.

3.2.1 FEM model with non-segmented magnets

The model was developed using the script editor available in SIMULIA Opera 3D Modeller. The resulting FEM model consists of 501547 elements.

Figure 3.3 shows a frontal view of the complete geometry. For clarity, the air-gap regions and the Carrier frame have been hidden in order to better highlight the main components of the BM-CMG model.

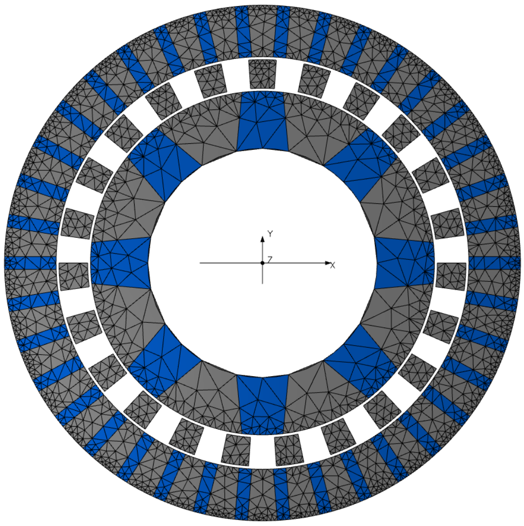

Figure 3.3: FEM model of BM-CMG without segmentation.

According to the software documentation, in order to perform transient electromagnetic simulations with moving parts, the air-gap regions between static and rotating components must be divided into three subregions. Figure 3.4 illustrates an example of this decomposition for the gap between the Sun and the Carrier.

The two outer subregions are assigned to the adjacent moving and stationary domains, respectively, while the central region represents the actual interface used by the solver to handle the relative motion between parts.

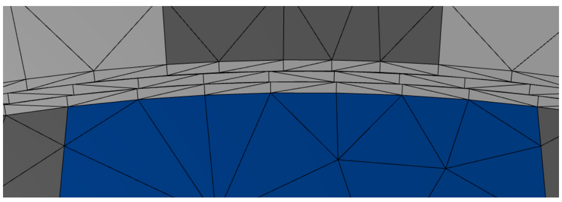

Figure 3.4: Air-gap between Sun (bottom) and Carrier (above) rotors.

To limit the total number of elements in the model, a structured mesh based on hexahedral or prismatic elements (HEX/PRISM) was adopted in the air-gap regions, instead of a tetrahedral mesh. This choice is motivated by both accuracy and computational efficiency.

In particular, prismatic elements are aligned along the thickness of the air-gap and are therefore more effective in capturing the magnetic flux density gradients with a reduced number of elements. In contrast, tetrahedral elements have arbitrary orientation, requiring a significantly larger number of elements to achieve comparable accuracy.

Moreover, since Opera performs a surface remeshing at each time step in transient simulations with motion, the use of prismatic elements leads to a faster remeshing process due to their simpler topology.

3.2.2 FEM model with segmented magnets

In this section, the model with segmented magnets is presented. The modelling approach described in the previous subsection remains applicable, and the same assumptions are retained.

The only difference between the two configurations lies in the segmentation of the PMs of both rotors.

To implement these segmentations, a thin insulating layer of thickness $ad = 0.1\,mm$ was inserted between the magnet components. The magnetization direction of each individual segment remains unchanged: $\mathbf{M} = M\mathbf{e}_\theta$.

In Table 3.2 are listed the parameters used to model the segmentation of the magnets.

Parameter	Symbol	Value	Unit
insulating layer thickness	ad	0.1	mm
mag. sun axial segmentation	ax_{SUN}	5	-
mag. sun radial segmentation	rd_{SUN}	1	-
mag. ring axial segmentation	ax_{RING}	1	-
mag. ring. radial segmentation	rd_{RING}	3	-

Table 3.2: Parameters for segmented magnets in BM-CMG model.

Figures 3.5a and 3.5b show the segmentation (highlighted in orange) of the Sun and Ring PMs, respectively, as defined by the parameters reported in Table 3.2.

The choice of the directions of segmentations will be justified in the next chapter (Section 4.2), based on the analysis of the current density distributions within the PM arrays of both rotors.

The developed model is characterized by a total number of 668623 finite elements. Compared to the FEM model with non-segmented PMs, 167076 additional elements

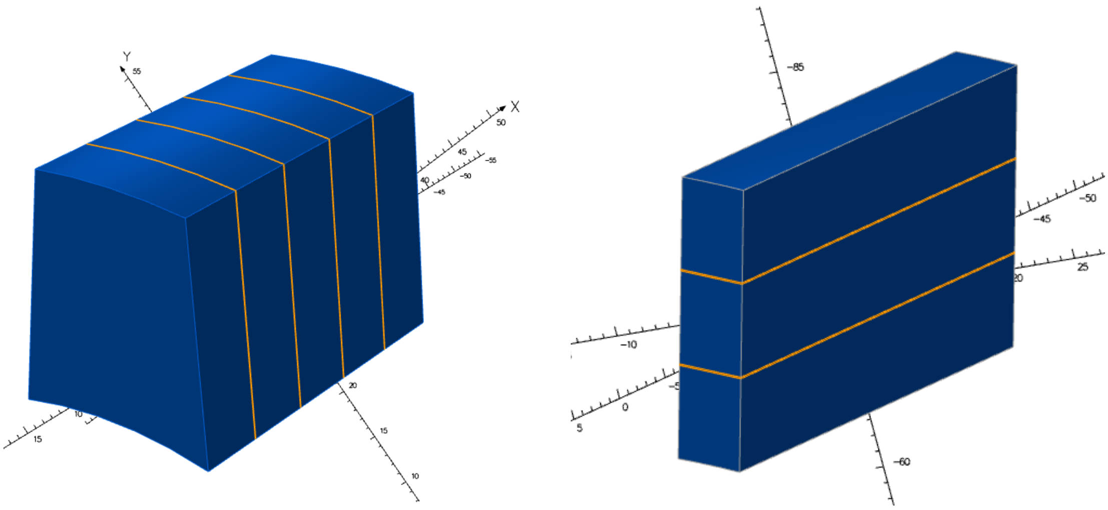

(a) Segmented PM of the Sun rotor. **(b)** Segmented PM of the Ring rotor.

Figure 3.5: Segmentation of PMs of both rotors.

are introduced due to the final volume mesh for the intermediate insulating layers adopted in the segmented configuration.

3.2.3 Material properties

With regard to the material properties, the values reported in Table 3.3 have been adopted in accordance with the assumptions introduced in Section 2.6.2.

In particular, the lamination of the yokes (for both rotors) and the ferromagnetic poles of the carrier are modelled by imposing zero electrical conductivity, i.e. $\sigma_{y,ip} = 0\,\mathrm{S/m}$, in order to neglect eddy current effects in these components.

The PMs, on the other hand, are assigned an electrical conductivity of $\sigma_m = 0.65 \cdot 10^6\,\mathrm{S/m}$, allowing the evaluation of eddy currents losses within them.

Concerning the magnetic properties, the relative permeabilities are defined consistently with the analytical model. In particular, the ferromagnetic regions are assumed to have very high permeability ($\mu_{y,ip,rel} = 1 \cdot 10^6$), approximating the condition $\mu_{Fe} \to \infty$, while the permanent magnets are modelled with $\mu_{m,rel} = 1$.

The material labelled as "Air" was adopted to model the surrounding region of the device, the air-gaps between the different components, and the insulating layers introduced between the segmented PMs in the corresponding FEM model. The same material was also assigned to the carrier frame in order to electrically and magnetically isolate the ferromagnetic pole pieces from each other.

Finally the magnitude of the residual flux density of the PMs is set to $B_r = 1.2\,\mathrm{T}$.

Material	electrical conductivity	rel. magnetic permeability
Iron	$\sigma_{y,ip} = 0\,S/m$	$\mu_{y,ip,rel} = 1 \cdot 10^6$;
NdFeB	$\sigma_m = 0.65 \cdot 10^6\,S/m$	$\mu_{m,rel} = 1$
Air	$\sigma_{air} = 0\,S/m$	$\mu_{air} = 1$

Table 3.3: Material properties of the BM-CMG model.

3.3 Simulation Setups

Two different simulation setups were adopted in order to evaluate the maximum transmissible torque of the model and the eddy currents losses within the PMs.

In both cases, steady-state transient electromagnetic simulations were performed by imposing the angular velocities of the model components (Sun, Ring, and Carrier). This approach, particularly relevant for the evaluation of eddy currents losses, avoids the need to model the mechanical transient behavior associated with rotor inertia, thus allowing a direct assessment of electromagnetic quantities under steady operating conditions.

3.3.1 Maximum Torque Transmissible

The adopted approach follows the procedure described in Section 2.8.2.

The angular velocity of the Ring rotor was set to zero, while the Carrier was assumed to be stationary.

The imposed kinematics consists of a 90° rotation of the Sun rotor at a constant rotational frequency of $f_s = 15000\,\mathrm{rpm}$. The corresponding angular velocity is:

$$\omega_s = 2\pi \cdot \frac{f_s}{60} = 1570.80\,\mathrm{rad/s} \tag{3.3}$$

Since the Sun rotor is characterized by $p_s = 4$ pole pairs, a mechanical rotation of 90° is sufficient to capture the complete torque-angle characteristic, as the torque profile is periodic with a period equal to $360°/p_s = 90°$.

In order to obtain a sufficiently dense sampling of the torque-angle curve, the simulation was discretized into 90 steps, corresponding to an angular increment of 1° per time step. The resulting time step t_{step} is given by:

$$t_{step} = t_{rev} \cdot \frac{1}{360} = 1.11 \cdot 10^{-5}\,\mathrm{s} \tag{3.4}$$

where t_{rev} is the duration of one complete revolution of the Sun rotor at the imposed rotational speed:

$$t_{rev} = \frac{60}{f_s} = 4 \cdot 10^{-3}\,\mathrm{s} \tag{3.5}$$

3.3.2 Eddy Currents on PMs

For the evaluation of eddy currents losses, the kinematics of the magnetic gear were defined by imposing again ω_s of Equation (3.3) to the Sun rotor. Using the gear transmission ratio τ, the angular velocity of the Ring rotor is obtained as:

$$\begin{aligned} \tau &= -\frac{p_r}{p_s} = -4.75 \\ \omega_r &= \frac{\omega_s}{\tau} = -330.70\,\mathrm{rad/s} \end{aligned} \tag{3.6}$$

Using the reference system introduced in section 2.1, the Sun during the simulation will rotate in a counter-clock wise direction while the Ring rotor will rotate in a clock-wise direction.

The electromagnetic field and the induced current density distributions were computed over one full revolution of the Sun rotor t_{rev}. Simulating one complete revolution is sufficient to evaluate the average power dissipation by averaging the instantaneous losses over the considered time steps.

The simulation was discretized into 72 time steps, corresponding to an angular increment of 5° of Sun rotation. The resulting time step is:

$$t_{step} = t_{rev} \cdot \frac{5}{360} = 5.56 \cdot 10^{-5}\,\mathrm{s} \tag{3.7}$$

This level of discretization represents a compromise between computational time and accuracy. It ensures an adequate resolution of the interaction between the PMs and the ferromagnetic pole pieces of the Carrier, while keeping the simulation time within reasonable limits. A smaller time step would further improve the accuracy, at the expense of a significantly increased computational time.

Chapter 4

Simulation Results

This chapter presents the results obtained from the numerical simulations and is divided into two main sections. The first section is devoted to the configuration with non-segmented PMs and includes the evaluation of the maximum transmissible torque of the coaxial magnetic gear. The second section focuses on the segmented PMs configuration and highlights the effects of magnet segmentation on the electromagnetic behavior of the device.

The magnetic field distribution is investigated both within the two air-gaps and inside the PMs of the Sun and Ring rotors. Furthermore, the collected data are post-processed in the cylindrical reference system introduced in Section 2.1, allowing the magnetic flux density vector to be decomposed into its radial and tangential components. This approach provides a more detailed understanding of the field distribution and its temporal evolution during operation.

Regarding the eddy currents analysis, the current density distribution within the PMs is first examined in order to identify the regions where the induced currents are mainly concentrated. Based on these observations, the temporal evolution of the current density is evaluated at representative locations on the magnet surfaces, corresponding to the areas of greatest interest for the characterization of the eddy currents phenomena.

4.1 Non-Segmented Magnets Configuration

Here the results concerning the simulation of BM-CMG without segmentation of PMs are discussed. The interaction between the magnetic field of the PMs of both rotors with the iron poles of the Carrier is described using some time steps of the simulation.

4.1.1 Magnetic Field Distributions

The global magnetic field distribution is shown in Figure 4.1. The figure reports the magnetic flux density vector field $\mathbf{B}$ evaluated on the plane $z = 0$, corresponding to the middle of the axial length of the CMG.

The outlines highlighted in the figure identify the PMs of the Sun and Ring rotors, as well as the ferromagnetic pole pieces of the Carrier located between them.

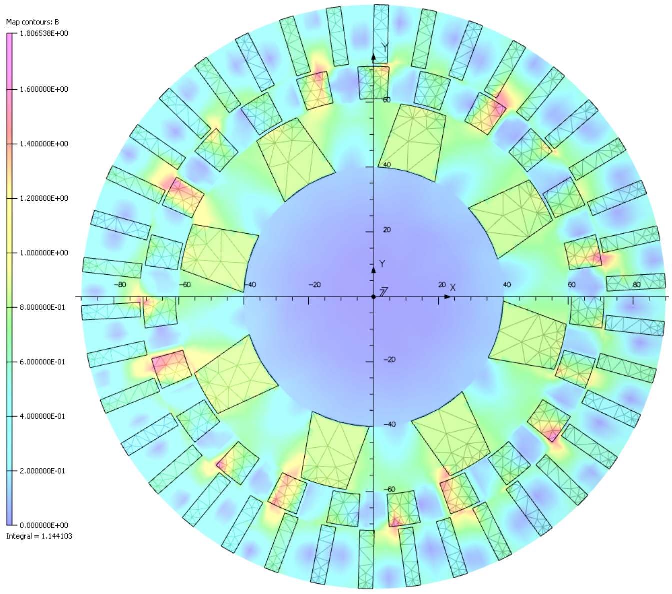

Figure 4.1: Magnetic flux density distribution evaluated at $z = 0$.

In order to provide a more detailed visualization of the magnetic field distribution, a magnified view is reported in Figure 4.2. The purple arrows indicate the direction of the magnetic flux density vector throughout the components of the CMG, while their magnitude is proportional to the intensity of the vector field $\mathbf{B}$.

It can be clearly observed that the ferromagnetic pole pieces magnetically couple the PMs of the Sun and Ring rotors having opposite magnetization directions $\mathbf{M}$.

Moreover, it can be noticed that the PMs of the Ring rotor do not exhibit the same flux density magnitude $\mathbf{B}$, as indicated by the non-uniform lengths of the purple arrows within them. In contrast, the PMs of the Sun rotor show arrows of comparable magnitude, indicating a more uniform flux density distribution. A detailed discussion of this phenomenon is provided in Section 4.1.2.

Both figures refer to the same simulation instant ($t = 3.33 \cdot 10^{-4}$ s).

Now considering air-gaps, their magnetic field distribution is analysed in terms of the magnitude of $\mathbf{B}$ and its decomposition into the radial and tangential components, B_ρ and B_θ, respectively, according to the cylindrical reference system introduced

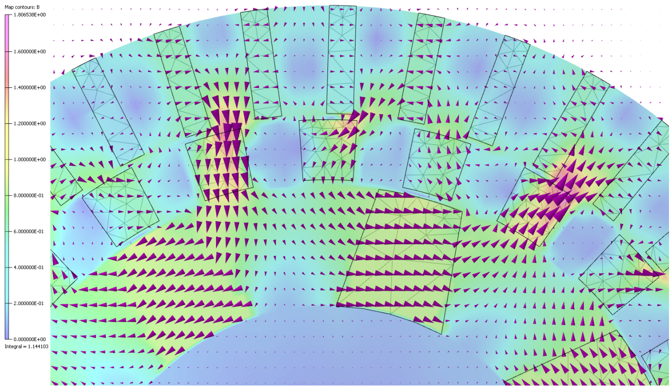

Figure 4.2: Zoomed view of the magnetic flux density vector field at $z = 0$.

in Section 2.1.

The magnetic field quantities were evaluated at a point located at the middle of each air-gap, over and under an iron pole of the Carrier as indicated by the orange markers in Figure 4.3.

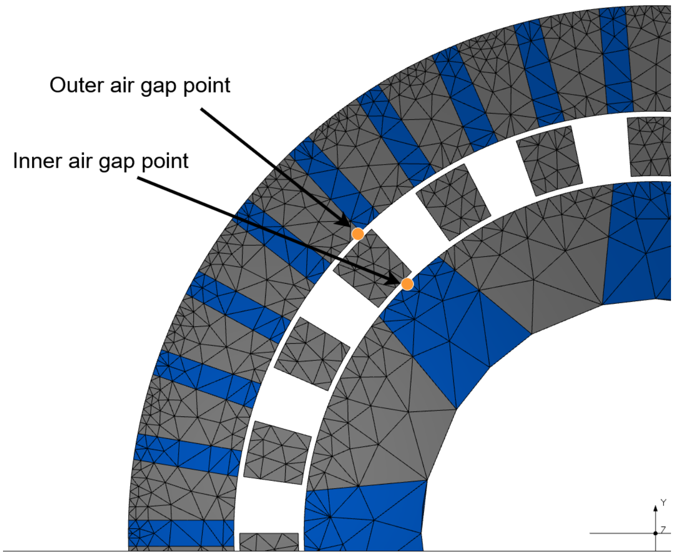

Figure 4.3: Evaluation points adopted for the magnetic field analysis in the air-gaps.

The magnetic flux density distributions in the air-gap between the Sun and Carrier rotors are reported in Figures 4.4a, 4.4b, and 4.4c.

It can be observed that the radial component B_ρ is approximately one order of magnitude larger than the tangential component B_θ. As a consequence, the variations in the magnitude of the magnetic flux density are mainly governed by the radial component. This indicates that the magnetic field distribution within the inner air-gap is predominantly radial.

The magnetic flux density distributions in the air-gap between the Ring and Carrier rotors are shown in Figures 4.4d, 4.4e, and 4.4f.

The radial and tangential components exhibit the same order of magnitude as observed in the inner air-gap. Therefore, the magnetic field distribution in the outer air-gap can be considered again to vary significantly in the radial direction.

4.1.2 Local Field Analysis in Magnets

The evaluation of the magnetic field distribution within the PMs of both the Sun and Ring rotors was carried out by considering one representative PM for each rotor and plotting, as in the previous section, the magnitude of $\mathbf{B}$ together with its decomposition into the radial and tangential components, B_ρ and B_θ, respectively. The reported graphs describe the time evolution of these quantities evaluated at the centre of mass of the selected PMs.

Starting from the PM of the inner rotor, Figure 4.5a shows the magnetic field distribution over its surface. The evolution of $\mathbf{B}$, B_ρ, and B_θ is reported in Figures 4.5b, 4.5c, and 4.5d.

Considering that ω_s is directed along the positive z axis, the Sun rotor rotates counter clockwise. The magnetization vector $\mathbf{M}$ associated with the considered PM (represented by the purple arrows in the figure) is oriented opposite to the rotation direction of the rotor. This behavior is confirmed by the results reported in Figures 4.5d and 4.5c: the tangential component B_θ is negative, while the radial component B_ρ remains almost negligible.

The three graphs do not show any substantial variation in the magnetic field values, apart from small oscillations. It can therefore be concluded that the magnetic field distribution within the PMs of the Sun rotor remains substantially unchanged throughout the entire simulation.

Shifting the attention to a PM of the outer rotor, Figure 4.6a shows the magnetic field distribution over its surface. Following the same approach adopted for the Sun rotor, Figures 4.6b, 4.6c, and 4.6d report the time evolution of the magnetic field and of its components evaluated at the centre of mass of the selected Ring rotor PM.

Considering that ω_r is directed along the negative z axis, the Ring rotor rotates clockwise, i.e. opposite to the Sun rotor. The magnetization vector $\mathbf{M}$ associated with the considered PM is again oriented opposite to the rotation direction of the rotor. This is confirmed by the results shown in Figures 4.6d and 4.6c, where B_θ assumes positive values while B_ρ remains close to zero.

In contrast with the behavior observed for the PM of the inner rotor, and

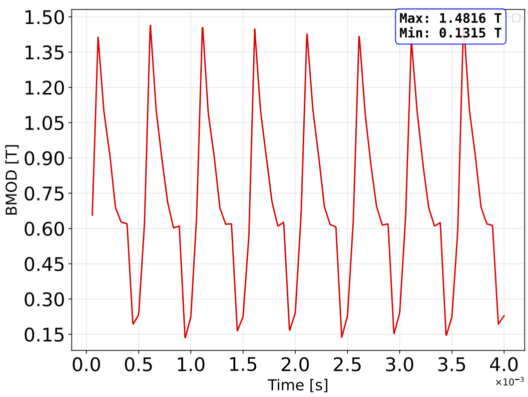

(a) Magnitude - Inner Air-Gap.

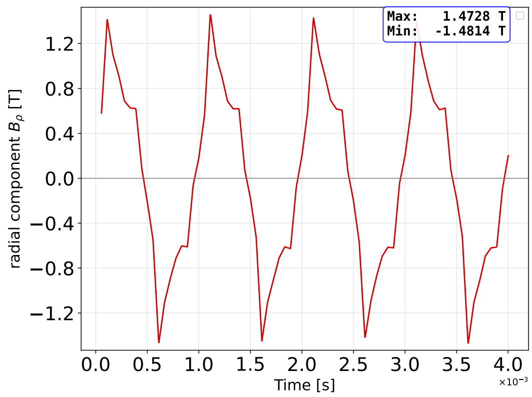

(b) Radial component - Inner Air-Gap.

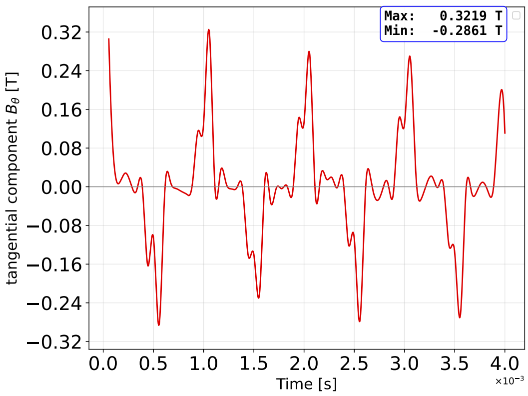

(c) Tangential component - Inner Air-Gap.

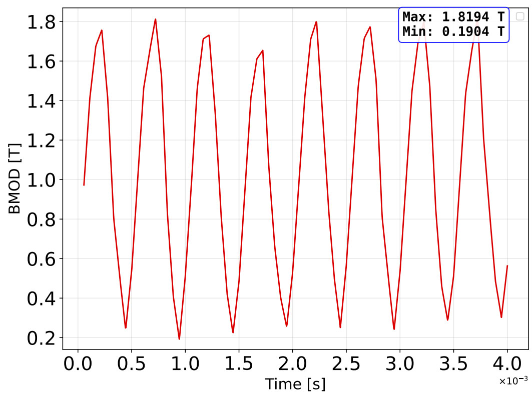

(d) Magnitude - Outer Air-Gap.

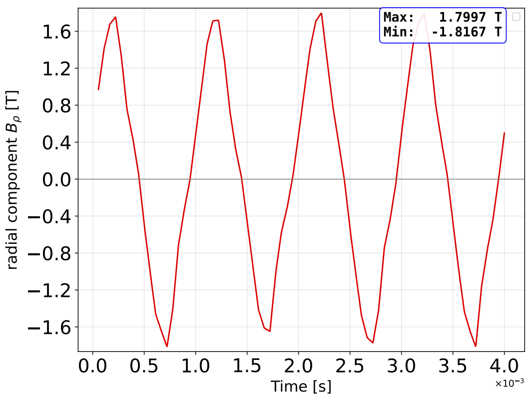

(e) Radial component - Outer Air-Gap.

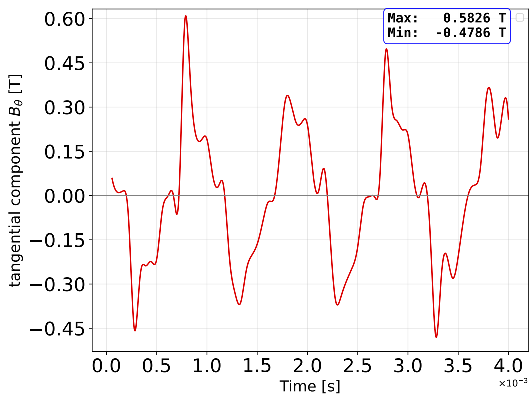

(f) Tangential component - Outer Air-Gap.

Figure 4.4: Magnetic flux density analysis as a function of time for the inner and outer air-gaps.

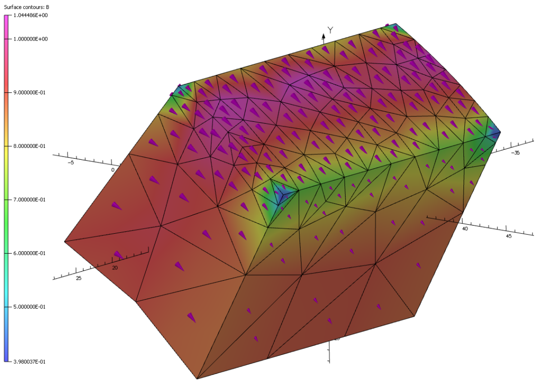

(a) Magnetic field distribution - Sun PM at $t_{step} = 1.11 \cdot 10^{-4}$ s.

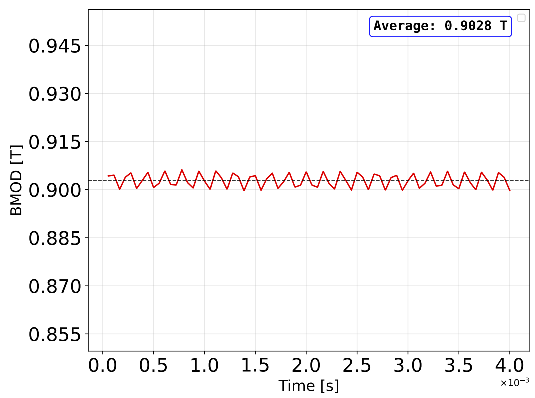

(b) Magnitude of the magnetic flux density - Sun PM.

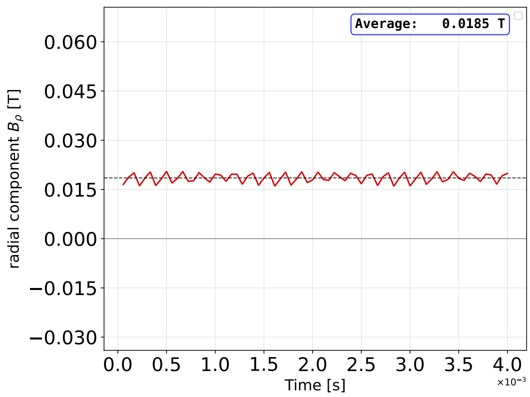

(c) Radial component of the magnetic flux density - Sun PM.

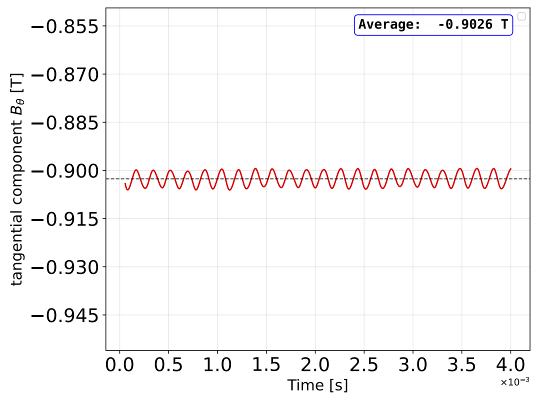

(d) Tangential component of the magnetic flux density - Sun PM.

Figure 4.5: Magnetic field distribution on the surface of a PM of the Sun rotor and the Magnetic flux density analysis as a function of time in its centre of mass.

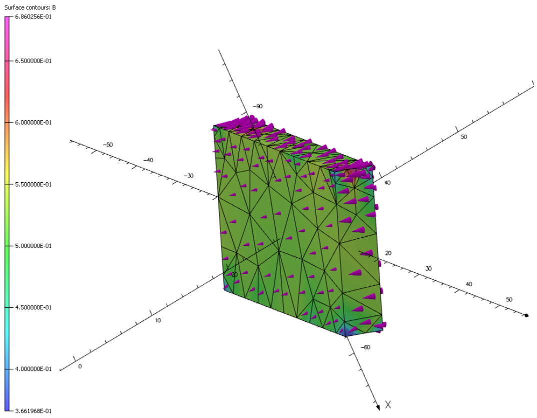

(a) Magnetic field distribution - Ring PM at $t_{step} = 1.11 \cdot 10^{-4}$ s.

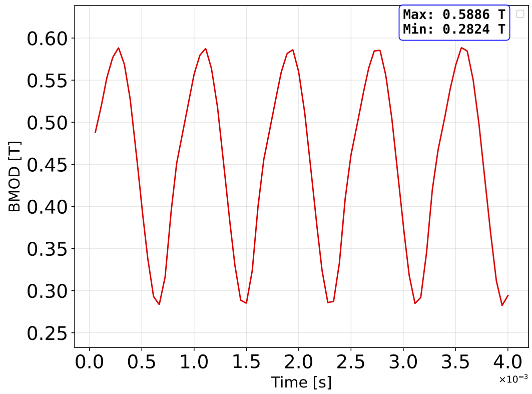

(b) Magnitude of the magnetic flux density - Ring PM.

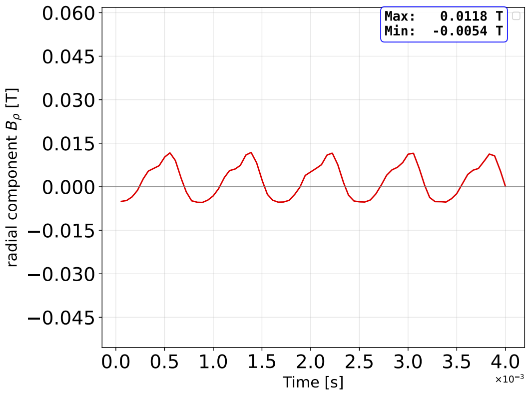

(c) Radial component of the magnetic flux density - Ring PM.

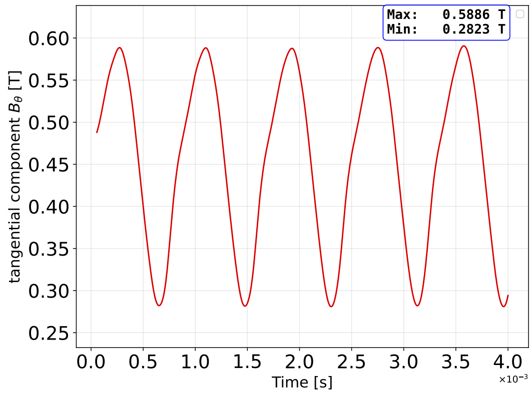

(d) Tangential component of the magnetic flux density - Ring PM.

Figure 4.6: Magnetic field distribution on the surface of a PM of the Ring rotor and the Magnetic flux density analysis as a function of time in its centre of mass.

consistently with the observations previously discussed in Section 4.1.1, Figure 4.6b shows that the magnetic field inside the Ring rotor PM is not constant but oscillates with variations of approximately 0.3 T.

4.1.3 Maximum transmissible torque of the model

Following the strategy described in Section 3.3.1, the EMT acting on both rotors was evaluated as a function of the angular position of the Sun rotor θ_{sun}. The obtained results are reported in Figure 4.7a.

It can be observed that the simulation starts from a condition close to the maximum transmissible torque. Both torque curves exhibit a periodic behavior with a period of approximately 90° (about 1.57 rad), consistently with the periodicity imposed by the $p_s = 4$ pole-pair configuration of the Sun rotor.

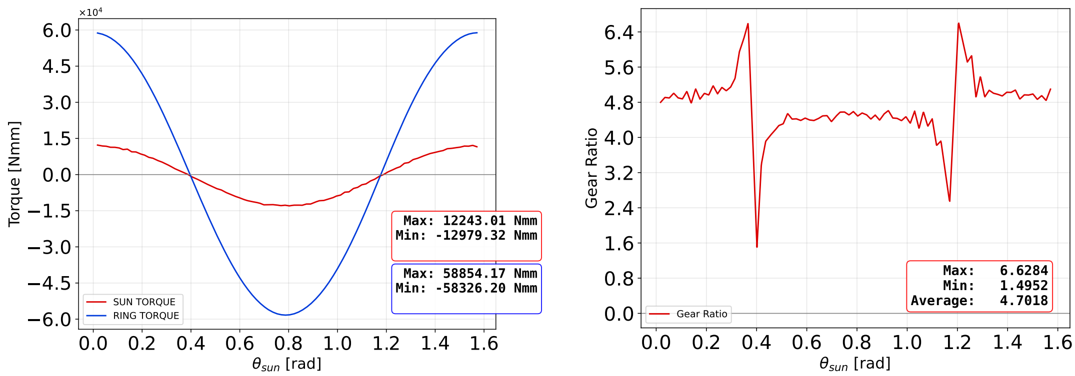

(a) Electromagnetic torques of Sun and Ring rotors as a function of θ_{sun}.

(b) Instantaneous gear ratio as a function of θ_{sun}.

Figure 4.7: Torque-angle characteristic and instantaneous gear ratio of the analyzed CMG.

The torque amplitudes obtained for the Ring rotor are significantly higher than those associated with the Sun rotor, consistently with the magnetic gear transmission ratio. Figure 4.7b reports the instantaneous gear ratio evaluated during the simulation. Although the ratio exhibits noticeable oscillations, its average value remains very close to the theoretical transmission ratio of the magnetic gear.

Furthermore, the instantaneous evaluation of the transmission ratio is strongly affected by numerical discretization errors associated with the transient FEM solution.

Nevertheless, the mean value of the obtained ratio is equal to approximately 4.70, which is in very good agreement with the theoretical transmission ratio $\tau = 4.75$, thus confirming the correct operation of the proposed CMG model.

4.1.4 Eddy Current Distribution in PMs

The distribution of eddy currents within the same representative PMs selected for the inner and outer rotors is presented in this section.

Starting from the PM of the Sun rotor, Figure 4.8a shows the surface distribution of the current density vector **J**. The purple arrows indicate the direction of the induced currents, while their dimensions are proportional to the magnitude of **J**.

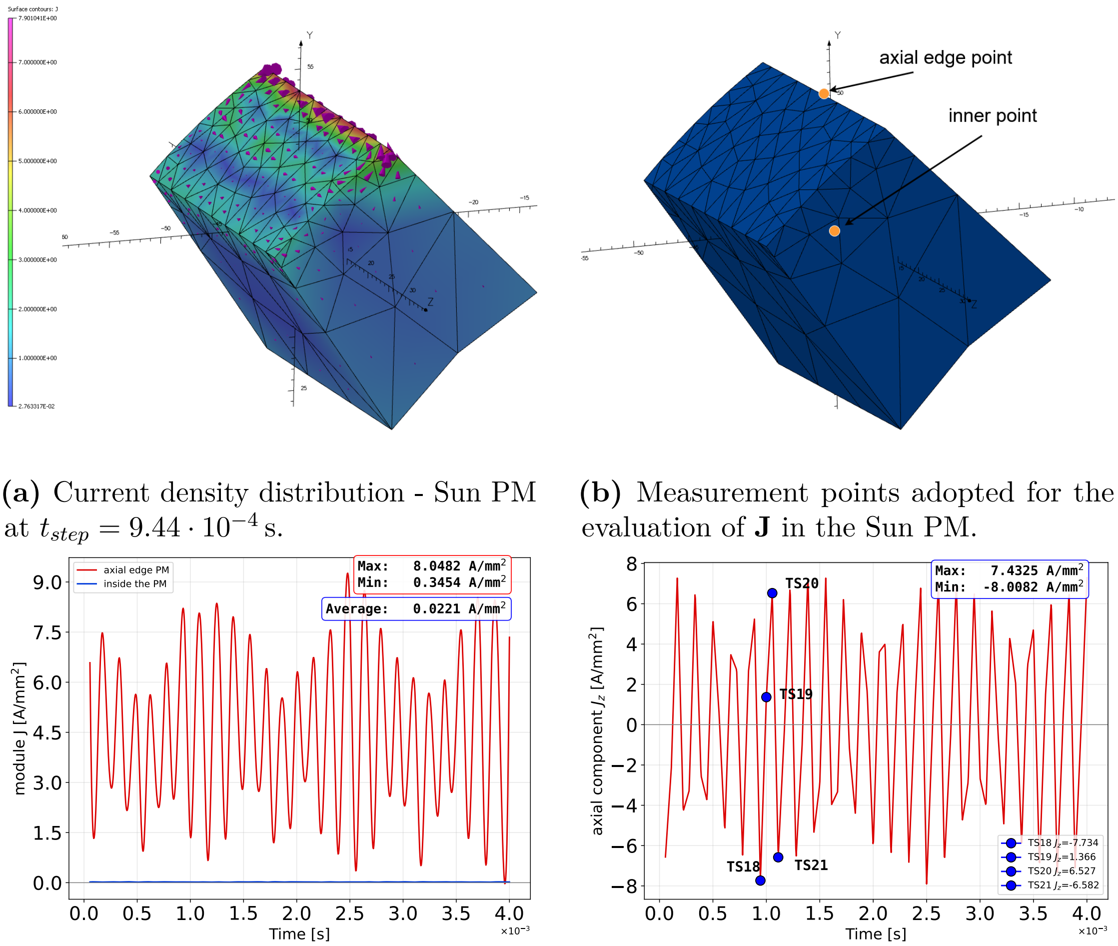

(a) Current density distribution - Sun PM at $t_{step} = 9.44 \cdot 10^{-4}$ s.

(b) Measurement points adopted for the evaluation of **J** in the Sun PM.

(c) Magnitude of the Current density - Sun PM.

(d) Axial component of the Current density - Sun PM.

Figure 4.8: Eddy currents distribution of a PM of the Sun rotor and the current density analysis as a function of time.

It can be clearly observed that the induced currents within the Sun PM are mainly concentrated on the upper surface facing the Carrier and its ferromagnetic pole pieces. Consequently, the eddy currents are predominantly distributed over an axial-tangential plane ($\theta - z$ plane).

Moreover, the current distribution does not form a single closed loop over the entire upper surface. Instead, two localized loops with opposite circulation directions can be identified, as visible in Figure 4.8a.

Considering the observed current distribution, the magnitude of **J** was evaluated at two different locations within the Sun PM. Figure 4.8b illustrates the adopted measurement points: the first one is located on the right axial edge of the upper surface, while the second one is positioned inside the PM volume.

The temporal evolution of the current density magnitude at these locations is reported in Figures 4.8c and 4.8d. The blue curve in the former one shows that the magnitude of **J** inside the magnet remains almost negligible throughout the simulation, confirming that the eddy currents are mainly confined near the upper surface.

Furthermore, Figure 4.8d shows that the axial component J_z evaluated at the right axial edge periodically changes sign, with an oscillatory behavior occurring approximately every three time steps. In particular, the time steps from 18 to 21 are highlighted in the figure, together with the corresponding values reported in the lower-right corner of the graph. It can be observed that the negative peak reached at time step 18 evolves toward the negative peak at time step 21, with a current reversal occurring at time step 19 and 20.

This behavior is directly related to the presence of $n_s = 23$ ferromagnetic pole pieces in the Carrier, which are spatially distributed with an angular pitch of 15.65°. Since each simulation time step corresponds to a mechanical rotation of 5° of the Sun rotor (Section 3.3.2), the inversion of the surface current direction within the Sun PM is expected to occur approximately every three time steps.

Proceeding with the analysis of the PM belonging to the Ring rotor, Figure 4.9a shows the surface distribution of the current density vector **J**. The purple arrows indicate the direction of the induced currents, while their dimensions are proportional to the magnitude of **J**.

The induced currents within the Ring PM are mainly distributed along the radial and axial surfaces of the magnet. The surfaces are identified according to the direction of their normal vectors. In Figure 4.9a, one of the axial surfaces is visible in the foreground, while one of the radial surfaces can be observed on the upper side of the PM.

Unlike the case of the Sun rotor PMs, where two current loops were observed, the Ring PM exhibits a single current loop distributed over the four external surfaces of the PM.

Figure 4.6 previously showed that the tangential component B_θ undergoes significant oscillations within the Ring PM. By considering the current loop distribution shown in Figure 4.9a, it can be concluded that these eddy currents directly contribute to such oscillations, since the magnetic field generated by the induced currents is mainly oriented along the tangential direction, as the internal magnetic field of the PM.

The magnitude of **J** was evaluated at two different locations within the Ring PM.

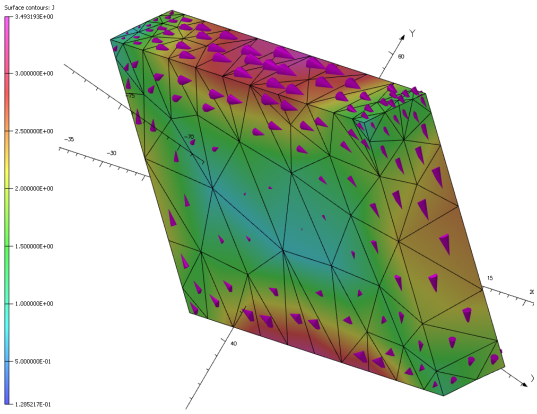

(a) Current density distribution - Ring PM at $t_{step} = 9.44 \cdot 10^{-4}$ s.

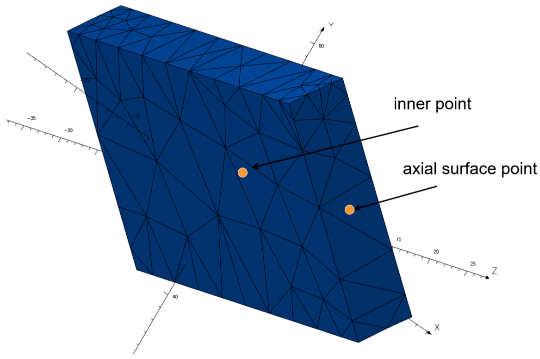

(b) Measurement points adopted for the evaluation of **J** in the Ring PM.

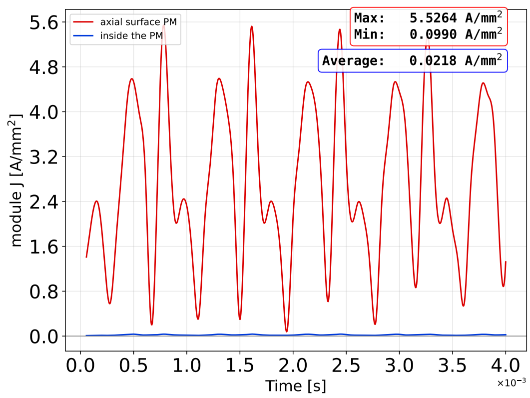

(c) Magnitude of the Current density - Ring PM.

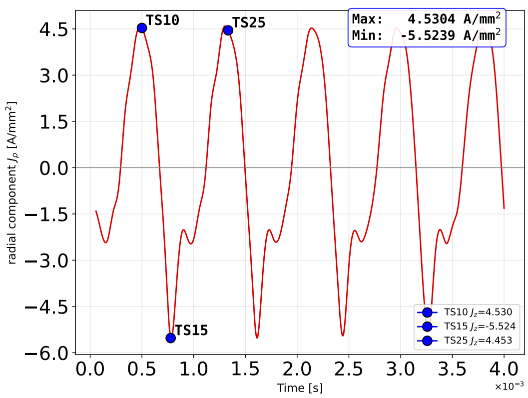

(d) Radial component of the Current density - Ring PM.

Figure 4.9: Eddy currents distribution of a PM of the Ring rotor and the current density analysis as a function of time.

Figure 4.9b illustrates the adopted measurement points: the first one is located at the middle of the front axial surface, while the second one is positioned inside the volume of the PM.

The temporal evolution of the current density magnitude at these locations is reported in Figures 4.9c and 4.9d. The blue curve in the former one shows that the magnitude of **J** inside the magnet remains almost negligible throughout the simulation, confirming that the eddy currents are mainly confined to the four external surfaces previously described.

Furthermore, Figure 4.9d shows that the radial component J_ρ, evaluated at the front axial surface, periodically changes sign, with an oscillatory behavior occurring approximately every 15 time steps. In particular, the time steps from 10 to 25 are highlighted in the figure, together with the corresponding values reported in the lower-right corner of the graph. It can be observed that the positive peak reached at time step 10 evolves toward another positive peak at time step 25, while a current reversal occurs around time step 15.

As previously discussed for the Sun rotor PM, this behavior is correlated with the interaction between the magnets and the ferromagnetic pole pieces of the Carrier. Considering that the Ring rotor rotates with angular velocity ω_r, the angular displacement performed during each simulation time step is:

$$|\theta_r| = \omega_r \cdot t_{step} \cdot \frac{180}{\pi} = 1.05^\circ \tag{4.1}$$

As said before the Carrier pole pieces are spaced by 15.65° and the radial current density component completes one full oscillation cycle after approximately:

$$|\theta_r| \cdot 15 = 15.75^\circ \tag{4.2}$$

which is consistent with the periodicity observed in Figure 4.9d.

4.1.5 Eddy Currents Losses in PMs

The eddy currents losses were evaluated according to the procedure described in Section 2.9. For each simulation time step, the integral in Equation 2.35 was computed by considering as integration domain the total volume occupied by the PMs of each rotor.

Figure 4.10 reports the instantaneous eddy currents power losses P_{eddy} evaluated over the 72 simulation time steps for both the Sun and Ring rotors.

It can be observed that the eddy currents losses are mainly concentrated within the PMs of the Ring rotor, while the contribution associated with the Sun rotor remains significantly lower throughout the simulation.

This behavior is directly related to the different magnetic field conditions experienced by the two sets of PMs. As discussed in Section 4.1.2, the magnetic

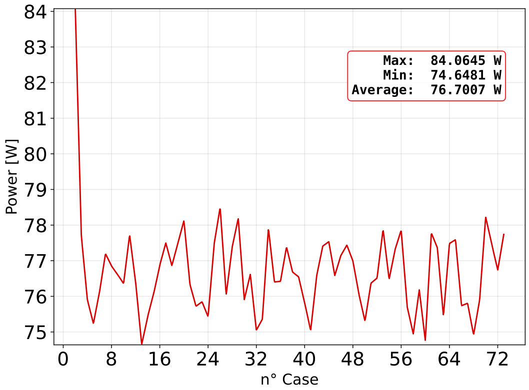

(a) Eddy currents losses in the PMs of the Sun rotor.

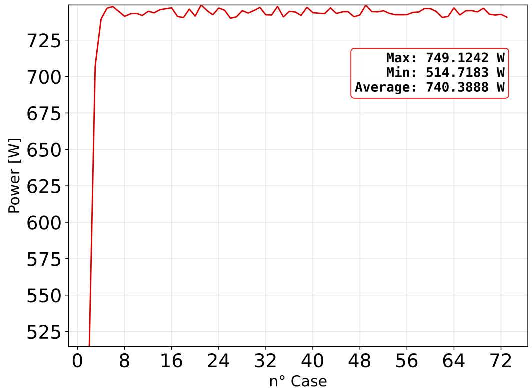

(b) Eddy currents losses in the PMs of the Ring rotor.

Figure 4.10: Instantaneous eddy currents losses evaluated within the PMs volumes of the two rotors.

field inside the Sun PMs remains almost constant during the entire simulation, with negligible variations in both magnitude and direction. Consequently, only limited time-varying magnetic flux is present within the conductive magnet volume, resulting in relatively small induced current densities.

Conversely, the PMs of the Ring rotor are subjected to significant oscillations of the magnetic field, particularly in the tangential component B_θ. These variations are caused by the modulation effect introduced by the ferromagnetic pole pieces of the Carrier rotor, which periodically alter the magnetic flux distribution seen by the outer PMs during operation.

Therefore, the higher losses observed in the Ring rotor can be attributed to the stronger time-varying magnetic field components acting inside its PMs.

Considering the average losses evaluated for both rotors, the total eddy currents losses associated with the configuration adopting non-segmented PMs can be estimated as:

$$P_{eddy} = 76.07 + 740.40 = 816.47\,\mathrm{W} \tag{4.3}$$

4.2 Segmented magnets configuration

This section presents the results obtained for the model with segmented PMs. The same candidate PMs previously selected for the non-segmented configuration were adopted for the analysis presented here.

In order to allow a direct comparison between the two configurations, the same measurement points introduced in Section 4.1.1 and Section 4.1.2 were used for the evaluation of the magnetic field distributions within the two air-gaps and inside the PMs of both rotors. Similarly, the same points defined in Section 4.1.4 were adopted for the analysis of the eddy currents distributions within the Sun and Ring PMs.

4.2.1 Magnetic Field Analysis in Air-Gaps and PMs

The magnetic flux density distribution remains substantially unchanged in the configuration adopting segmented PMs. Figure 4.11 reports the temporal evolution of the radial and tangential components, B_ρ and B_θ, respectively, for both air gaps.

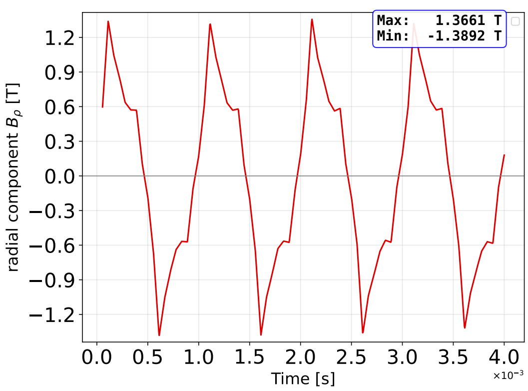

(a) Radial component - Inner gap

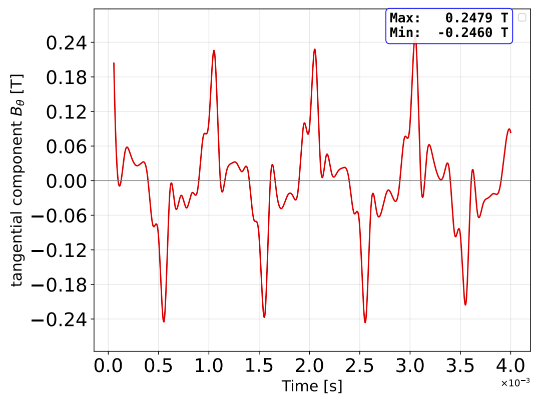

(b) Tangential component - Inner gap

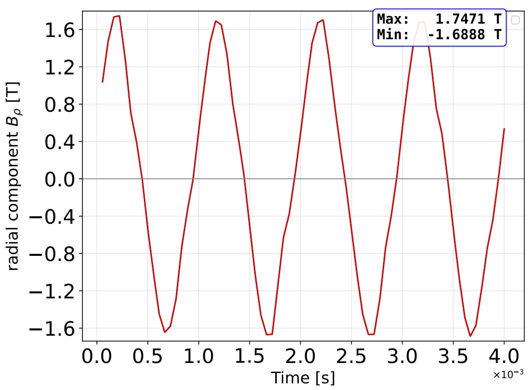

(c) Radial component - Outer gap

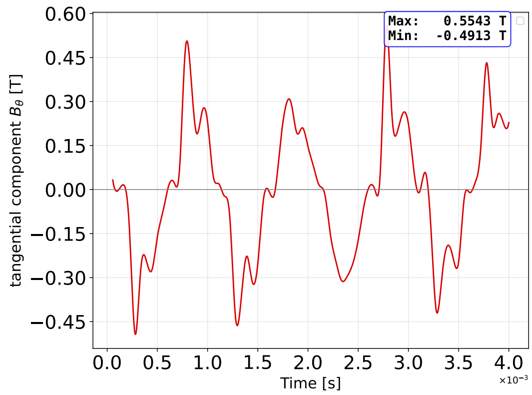

(d) Tangential component - Outer gap

Figure 4.11: Magnetic flux density analysis as a function of time for the inner and outer air-gaps.

A similar consideration can be made for the magnetic field distribution within the PMs of both rotors. The same qualitative behavior observed for the non-segmented configuration is maintained also in the segmented case.

In particular, the magnetic field distribution within the PMs of the Sun rotor remains substantially unchanged throughout the entire simulation, with only negligible local variations.

Conversely, the magnetic field inside the PMs of the Ring rotor is still characterized by an oscillatory behavior, with variations of approximately 0.3 T, similarly to what was previously observed in the non-segmented configuration.

In Figure 4.12 are depicted the component B_θ for both PMs.

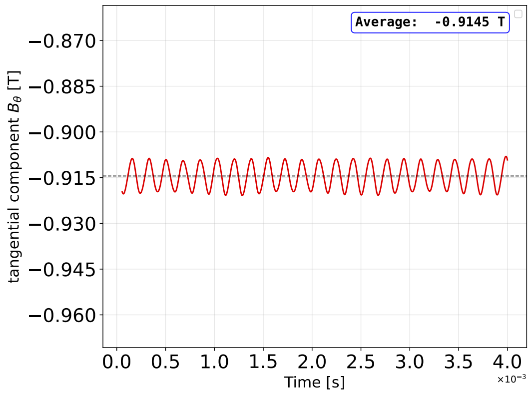

(a) Tangential component of the magnetic flux density - Sun PM.

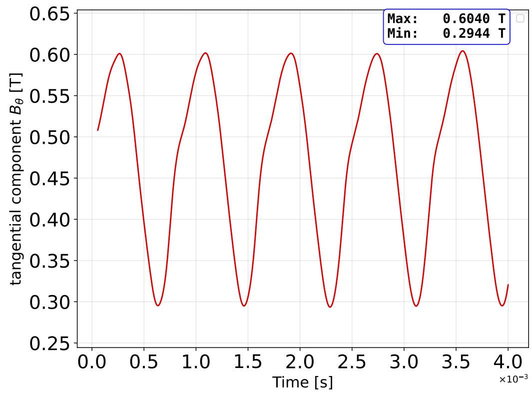

(b) Tangential component of the magnetic flux density - Ring PM.

Figure 4.12: Magnetic flux density analysis as a function of time in both PMs.

4.2.2 Eddy Currents Distributions in PMs

As discussed in Section 4.1.4, the eddy currents loops within the PMs of the Sun rotor mainly develop over axial-tangential planes. Consequently, the most effective way to interrupt the currents paths is to segment the magnets along their axial direction.

Conversely, the eddy currents loops observed within the PMs of the Ring rotor mainly develop over planes whose normal direction is tangential. Therefore, in this case, the most effective mitigation strategy consists in segmenting the magnets along their radial direction.

For convenience, the segmentation parameters already introduced in Table 3.2 are reported below:

- Sun magnets axial segmentation: $ax_{SUN} = 5$

- Ring magnets radial segmentation: $rd_{RING} = 3$

Starting from the PM of the Sun rotor, Figure 4.13a reports the results obtained from the simulations adopting the segmented configuration.

Each segment of the PM exhibits two opposite eddy currents loops. Similarly to the non-segmented case, the interaction with the ferromagnetic pole pieces of the Carrier rotor produces the same oscillatory behavior of the induced currents previously observed.

Figure 4.13c shows that the periodic oscillations described for Figure 4.8d remain substantially unchanged also in the segmented configuration.

However, segmentation produces a significant reduction in the magnitude of the induced currents density $\mathbf{J}$. In particular, the peak value decreases from $8.04\,\mathrm{A/mm^2}$ in the non-segmented configuration (Figure 4.8c) to $4.75\,\mathrm{A/mm^2}$ in the segmented case (Figure 4.13b).

This reduction can be explained by considering that the segmentation interrupts the conductive paths available for the circulation of eddy currents. By dividing the PM into smaller insulated volumes, the effective area enclosed by each current loop is reduced, leading to a corresponding reduction in the magnetic flux linked by the loop according to Faraday's law.

Following with the PM of the Ring rotor, Figure 4.14a reports the results obtained from the simulations adopting the segmented configuration.

Each segment of the Ring PM exhibits one eddy current loop distributed along the radial and axial surfaces of the magnet. Compared to the non-segmented configuration, the currents paths are now confined within smaller conductive regions due to the radial segmentation.

Although the positive peaks shown in Figure 4.14c occur at different time steps with respect to the non-segmented case reported in Figure 4.9d, the same oscillatory behavior of the induced currents is still observed. In particular, the periodicity of 15 time steps remains substantially unchanged.

Also in the case of the Ring PM, segmentation produces a significant reduction in the magnitude of the induced current density $\mathbf{J}$. In particular, the peak value decreases from $5.52\,\mathrm{A/mm^2}$ in the non-segmented configuration (Figure 4.9c) to $1.72\,\mathrm{A/mm^2}$ in the segmented configuration (Figure 4.14b).

4.2.3 Eddy Current Loss Reduction Analysis

With the same approach used in Section 4.1.5, here the eddy currents losses were evaluated for the segmented PM case.

Figure 4.15 reports the instantaneous eddy currents power losses P_{eddy} evaluated over the 72 simulation time steps for both the Sun and Ring rotors.

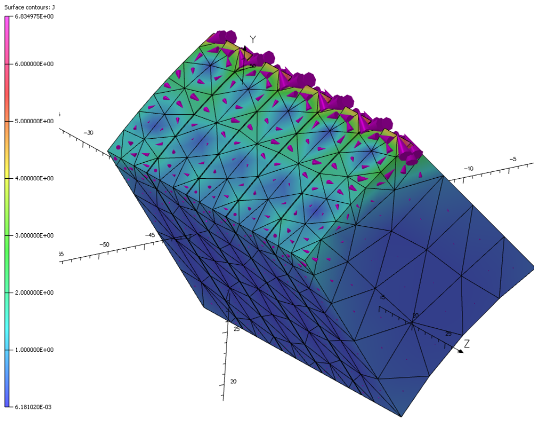

(a) Current density distribution - Sun PM at $t_{step} = 9.44 \cdot 10^{-4}$ s.

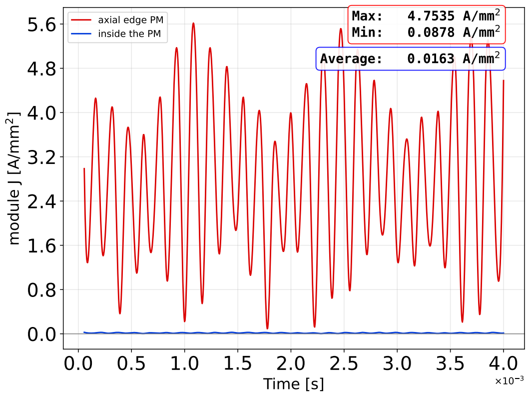

(b) Magnitude of the Current density - Sun PM.

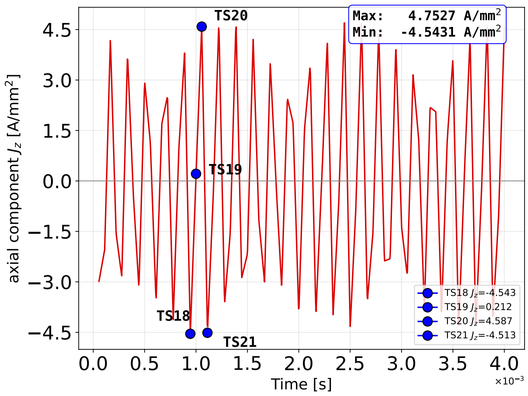

(c) Axial component of the Current density - Sun PM.

Figure 4.13: Eddy currents distribution of a PM of the Sun rotor and the current density analysis as a function of time.

Considering the average losses evaluated for both rotors, the total eddy currents losses associated with the configuration adopting non-segmented PMs can be estimated as:

$$P_{eddy} = 34.18 + 138.09 = 172.27\,\text{W} \tag{4.4}$$

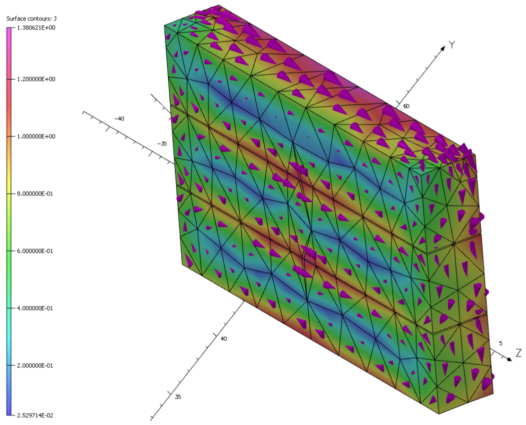

(a) Current density distribution - Ring PM at $t_{step} = 9.44 \cdot 10^{-4}$ s.

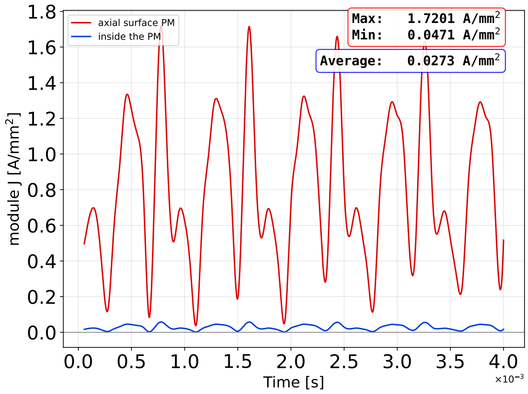

(b) Magnitude of the Current density - Ring PM.

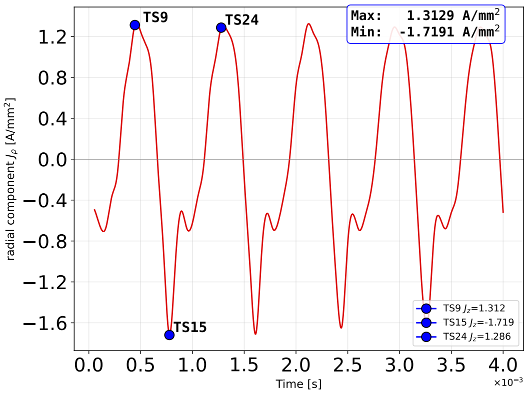

(c) Radial component of the Current density - Ring PM.

Figure 4.14: Eddy currents distribution of a PM of the Ring rotor and the current density analysis as a function of time.

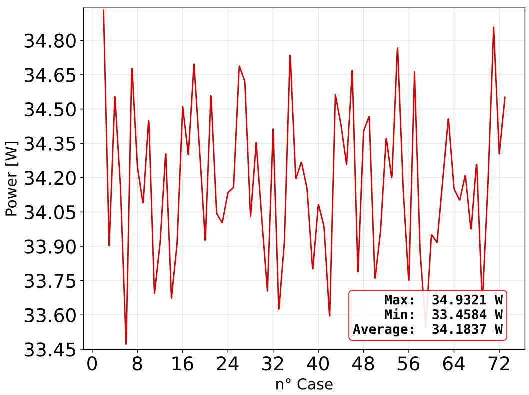

(a) Eddy current losses in the PMs of the Sun rotor.

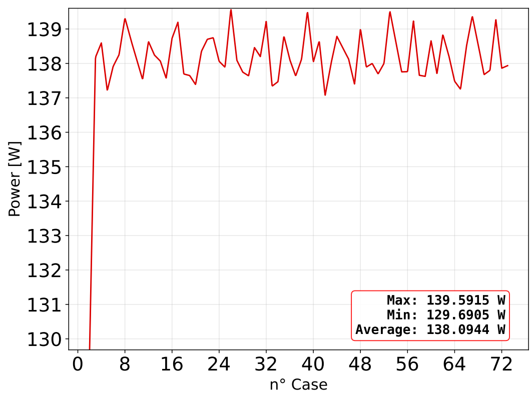

(b) Eddy current losses in the PMs of the Ring rotor.

Figure 4.15: Instantaneous eddy current losses evaluated within the PMs volumes of the two rotors.

Conclusions

The analysis of the eddy currents distributions revealed that the largest share of the losses is concentrated within the PMs of the Ring rotor. Consequently, particular attention should be devoted to the mitigation of losses in the outer rotor magnets. Although only $rd_{RING} = 3$ segments were adopted, a substantial reduction in the eddy-current losses was achieved, confirming that the selected segmentation direction successfully interrupts the dominant current paths responsible for power dissipation.

Overall, the results indicate that an appropriate segmentation of the Ring rotor magnets can significantly improve the efficiency of the CMG without appreciably affecting its magnetic field distribution and torque transmission capability. Therefore, magnet segmentation represents an effective design solution for reducing eddy-currents losses in high-speed BM-CMG

Bibliography

[1] Bo Yan, Xianglin Li, Xiuhe Wang, and Yubo Yang. «A review on the field-modulated magnetic gears: Development status, potential applications, and existent challenges». In: *IET Electric Power Applications* 18.1 (2024), pp. 1–19. DOI: `https://doi.org/10.1049/elp2.12365`. eprint: `https://ietresearch.onlinelibrary.wiley.com/doi/pdf/10.1049/elp2.12365`. URL: `https://ietresearch.onlinelibrary.wiley.com/doi/abs/10.1049/elp2.12365` (cit. on pp. 2, 6, 7).

[2] Kais Atallah, Jan Rens, Smail Mezani, and David Howe. «A Novel "Pseudo" Direct-Drive Brushless Permanent Magnet Machine». In: *IEEE Transactions on Magnetics* 44.11 (2008), pp. 4349–4352. DOI: `10.1109/TMAG.2008.2001509` (cit. on p. 2).

[3] K. Atallah and D. Howe. «A novel high-performance magnetic gear». In: *IEEE Transactions on Magnetics* 37.4 (2001), pp. 2844–2846. DOI: `10.1109/20.951324` (cit. on pp. 3, 22, 23).

[4] E. Gouda, S. Mezani, L. Baghli, and A. Rezzoug. «Comparative Study Between Mechanical and Magnetic Planetary Gears». In: *IEEE Transactions on Magnetics* 47.2 (2011), pp. 439–450. DOI: `10.1109/TMAG.2010.2090890` (cit. on p. 3).

[5] Hua-Yang Li, He Hao, Meng-Jia Jin, and Jian-Xin Shen. «Analytical Calculation of Magnetic Field Distribution in Magnetic Gears with Consequent-Pole Rotors by Subdomain Method». In: *2016 IEEE Vehicle Power and Propulsion Conference (VPPC)*. 2016, pp. 1–6. DOI: `10.1109/VPPC.2016.7791617` (cit. on pp. 5, 19, 20).

[6] Linni Jian and K. T. Chau. «A Coaxial Magnetic Gear With Halbach Permanent-Magnet Arrays». In: *IEEE Transactions on Energy Conversion* 25.2 (2010), pp. 319–328. DOI: `10.1109/TEC.2010.2046997` (cit. on pp. 5, 6).

[7] Libing Jing, Zhangxian Huang, Junlin Chen, and Ronghai Qu. «An Asymmetric Pole Coaxial Magnetic Gear With Unequal Halbach Arrays and Spoke Structure». In: *IEEE Transactions on Applied Superconductivity* 30.4 (2020), pp. 1–5. DOI: 10.1109/TASC.2019.2962687 (cit. on pp. 5, 6).

[8] Libing Jing, Jun Gong, Junlin Chen, Zhangxian Huang, and Ronghai Qu. «A Novel Coaxial Magnetic Gear With Unequal Halbach Arrays and Non-Uniform Air Gap». In: *IEEE Transactions on Applied Superconductivity* 30.4 (2020), pp. 1–5. DOI: 10.1109/TASC.2020.2968043 (cit. on pp. 5, 6).

[9] Yiduan Chen, Wei Nong Fu, Siu Lau Ho, and Huijuan Liu. «A Quantitative Comparison Analysis of Radial-Flux, Transverse-Flux, and Axial-Flux Magnetic Gears». In: *IEEE Transactions on Magnetics* 50.11 (2014), pp. 1–4. DOI: 10.1109/TMAG.2014.2327622 (cit. on p. 6).

[10] Luca Dimauro, Elvio Bonisoli, Mauro Velardocchia, Maurizio Repetto, Piergiorgio Alotto, Mattia Filippini, and Riccardo Torchio. «Magnetic gearbox for automotive power transmissions: An innovative industrial technology». In: *Engineering Science and Technology, an International Journal* 46 (2023), p. 101497. ISSN: 2215-0986. DOI: https://doi.org/10.1016/j.jestch.2023.101497. URL: https://www.sciencedirect.com/science/article/pii/S2215098623001751 (cit. on pp. 7–9, 26).

[11] Cheng-Tsung Liu, He-Yu Chung, and Chang-Chou Hwang. «Design Assessments of a Magnetic-Geared Double-Rotor Permanent Magnet Generator». In: *IEEE Transactions on Magnetics* 50.1 (2014), pp. 1–4. DOI: 10.1109/TMAG.2013.2279260 (cit. on pp. 9, 10).

[12] Chan-Bae Park, Seong-Hwi Kim, Jae-Hyeon Lim, Ik-Hyun Jo, Hyoung-Woo Lee, and Jae-Bum Lee. «Design Study of 800W-Class Hollow-Type Magnetic Geared Permanent Magnet Synchronous Motor for Industrial Robot Arm Application». In: *2024 IEEE 19th Conference on Industrial Electronics and Applications (ICIEA)*. 2024, pp. 1–6. DOI: 10.1109/ICIEA61579.2024.10665025 (cit. on pp. 10, 11).

[13] CARLOS Neves and Aly Flores Filho. «Magnetic Gearing Electromagnetic Concepts». In: *Journal of Microwaves, Optoelectronics and Electromagnetic Applications* 16 (Mar. 2017), pp. 108–119. DOI: 10.1590/2179-10742017v16i1874 (cit. on pp. 14, 16).

[14] O. Biro and K. Preis. «On the use of the magnetic vector potential in the finite-element analysis of three-dimensional eddy currents». In: *IEEE Transactions on Magnetics* 25.4 (1989), pp. 3145–3159. DOI: 10.1109/20.34388 (cit. on p. 18).

[15] E.E. Kriezis, T.D. Tsiboukis, S.M. Panas, and J.A. Tegopoulos. «Eddy currents: theory and applications». In: *Proceedings of the IEEE* 80.10 (1992), pp. 1559–1589. DOI: 10.1109/5.168666 (cit. on p. 18).

[16] Xiaoxu Zhang, Xiao Liu, Zhanfeng Song, and Zhe Chen. «Fast calculation of magnetic field distribution in magnetic gear for high torque application». In: *2016 XXII International Conference on Electrical Machines (ICEM)*. 2016, pp. 1742–1748. DOI: 10.1109/ICELMACH.2016.7732759 (cit. on pp. 19, 20, 22).

[17] Manh-Dung Nguyen, Woo-Sung Jung, Duy-Tinh Hoang, Yong-Joo Kim, Kyung-Hun Shin, and Jang-Young Choi. «Fast Analysis and Optimization of a Magnetic Gear Based on Subdomain Modeling». In: *Mathematics* 12.18 (2024). ISSN: 2227-7390. DOI: 10.3390/math12182922. URL: https://www.mdpi.com/2227-7390/12/18/2922 (cit. on p. 19).

[18] Luca Dimauro. «Power transmission systems: from traditional to magnetic gearboxes». PhD thesis. Torino, Italy: Politecnico di Torino, May 2021. URL: https://iris.polito.it/handle/11583/2903332 (cit. on pp. 24, 25).

[19] Herbert W Müller. *Epicyclic drive trains: Analysis, synthesis, and applications.* Wayne State University Press, 1982 (cit. on p. 25).

[20] Stefano Lovato, Giovanni Barosco, Ludovico Ortombina, Riccardo Torchio, Piergiorgio Alotto, Maurizio Repetto, and Matteo Massaro. «Experimental Analysis of a Coaxial Magnetic Gear Prototype». In: *Machines* 13.8 (2025). ISSN: 2075-1702. DOI: 10.3390/machines13080716. URL: https://www.mdpi.com/2075-1702/13/8/716 (cit. on p. 26).

[21] Jun-gang Wang and Zhi-liang Zeng. «Research on the dynamic behavior and dynamic stability mechanism of coaxial magnetic gear transmission system». In: *Journal of Engineering Mathematics* 155.1 (2025), pp. 1–27 (cit. on pp. 27, 28).

[22] Mohd Firdaus Mohd Ab Halim, Erwan Sulaiman, Raja Firdaus, and Azhan Rahman. «A NEW SPEED MULTIPLIER COAXIAL MAGNETIC GEAR». In: *Progress In Electromagnetics Research M* 93 (Jan. 2020), pp. 145–154. DOI: 10.2528/PIERM20040103 (cit. on p. 27).

[23] Mattia Filippini, Piergiorgio Alotto, Vincenzo Cirimele, Maurizio Repetto, Carlo Ragusa, Luca Dimauro, and Elvio Bonisoli. «Magnetic Loss Analysis in Coaxial Magnetic Gears». In: *Electronics* 8.11 (2019). ISSN: 2079-9292. DOI: 10.3390/electronics8111320. URL: https://www.mdpi.com/2079-9292/8/11/1320 (cit. on p. 27).

[24] Samith Sirimanna, Thanatheepan Balachandran, and Kiruba Haran. «A Review on Magnet Loss Analysis, Validation, Design Considerations, and Reduction Strategies in Permanent Magnet Synchronous Motors». In: *Energies* 15.17 (2022). ISSN: 1996-1073. DOI: `10.3390/en15176116`. URL: `https://www.mdpi.com/1996-1073/15/17/6116` (cit. on p. 29).

[25] Peter Sergeant and Alex Van den Bossche. «Segmentation of Magnets to Reduce Losses in Permanent-Magnet Synchronous Machines». In: *IEEE Transactions on Magnetics* 44.11 (2008), pp. 4409–4412. DOI: `10.1109/TMAG.2008.2001347` (cit. on p. 29).